Opposing authigenic controls on the isotopic signature of dissolved iron in hydrothermal plumes

A.J.M. Lough [a,b,*], J.K. Klar [b,1], W.B. Homoky [c], S.A. Comer-Warner [a,b,2], J.A. Milton [b], D.P. Connelly [a], R.H. James [b], R.A. Mills [b]

[a] National Oceanography Centre, European Way, Southampton SO14 3ZH, UK
[b] Ocean and Earth Science, National Oceanography Centre Southampton, University of Southampton, Southampton SO14 3ZH, UK
[c] Department of Earth Sciences, University of Oxford, South Parks Road, Oxford OX1 3AN, UK

Abstract

Iron is a scarce but essential micronutrient in the oceans that limits primary productivity in many regions of the surface ocean. The mechanisms and rates of Fe supply to the ocean interior are still poorly understood and quantified. Iron isotope ratios of different Fe pools can potentially be used to trace sources and sinks of the global Fe biogeochemical cycle if these boundary fluxes have distinct signatures. Seafloor hydrothermal vents emit metal rich fluids from mid-ocean ridges into the deep ocean. Iron isotope ratios have the potential to be used to trace the input of hydrothermal dissolved iron to the oceans if the local controls on the fractionation of Fe isotopes during plume dispersal in the deep ocean are understood. In this study we assess the behaviour of Fe isotopes in a Southern Ocean hydrothermal plume using a sampling program of Total Dissolvable Fe (TDFe), and dissolved Fe (dFe). We demonstrate that δ^{56}Fe values of dFe (δ^{56}dFe) within the hydrothermal plume change dramatically during early plume dispersal, ranging from $-2.39 \pm 0.05‰$ to $-0.13 \pm 0.06‰$ (2 SD). The isotopic composition of TDFe (δ^{56}TDFe) was consistently heavier than dFe values, ranging from $-0.31 \pm 0.03‰$ to $0.78 \pm 0.05‰$, consistent with Fe oxyhydroxide precipitation as the plume samples age. The dFe present in the hydrothermal plume includes stabilised dFe species with potential to be transported to the deep ocean. We estimate that stable dFe exported from the plume will have a δ^{56}Fe of $-0.28 \pm 0.17‰$. Further, we show that the proportion of authigenic iron-sulfide and iron-oxyhydroxide minerals precipitating in the buoyant plume exert opposing controls on the resultant isotope composition of dissolved Fe passed into the neutrally buoyant plume. We show that such controls yield variable dissolved Fe isotope signatures under the authigenic conditions reported from modern vent sites elsewhere, and so ought to be considered during iron isotope reconstructions of past hydrothermalism from ocean sediment records.

© 2017 The Authors. Published by Elsevier Ltd. This is an open access article under the CC BY license (http://creativecommons.org/licenses/by/4.0/).

Keywords: Iron isotopes; Hydrothermal plume; East Scotia Ridge; Isotope fractionation

* Corresponding author at: National Oceanography Centre, University of Southampton Waterfront Campus, European Way, Southampton SO14 3ZH, UK.

E-mail address: A.J.M.Lough@soton.ac.uk (A.J.M. Lough).

[1] Now at: LEGOS, Université de Toulouse, CNRS, CNES, IRD, UPS, 14 avenue Edouard Belin, 31400 Toulouse, France.
[2] Now at: Geography, Earth and Environmental Sciences, University of Birmingham, Edgbaston, Birmingham B15 2TT, UK.

1. INTRODUCTION

Iron (Fe) is a key micronutrient that often limits primary productivity in high nutrient low chlorophyll zones of the surface ocean and therefore has an indirect influence on the biological carbon pump (Martin, 1990). For this reason it is important to understand the biogeochemical cycle of Fe in the marine environment. Iron exhibits very low

solubility in seawater and hence is only present in pico- to nano-molar concentrations. A consequence of this is that Fe is a limiting nutrient in areas where other key nutrients are abundant, such as the Southern Ocean (Moore et al., 2013).

In contrast, the Fe content of hydrothermal vent fluids is in the μM to mM range (Elderfield and Schultz, 1996). The recent basin-scale sampling of the GEOTRACES program highlighted areas of increased dissolved Fe (dFe) concentration (>1 nM) extending for thousands of km away from mid-ocean ridges (Nishioka et al., 2013; Conway and John, 2014; Fitzsimmons et al., 2014; Resing et al., 2015). Hydrothermal vents had long been considered to have a negligible impact on ocean dFe due to extensive Fe mineral precipitation in the stock work, chimney features and hydrothermal plume (Elderfield and Schultz, 1996). On the other hand recent work suggests that 4–7.5% of hydrothermal Fe may be prevented from precipitating as Fe minerals by complexation with organic ligands (Bennett et al., 2008; Hawkes et al., 2013; Kleint et al., 2016). The distributions of dFe observed in the deep ocean are better reproduced in models by including a relatively significant flux of hydrothermal Fe to the deep ocean (Tagliabue, 2010). These observations suggest that hydrothermal vents represent an important and previously overlooked source of dFe to the oceans.

1.1. Fe in hydrothermal systems

As seawater circulates through the crust and undergoes alteration, Fe is leached from host rocks and the sea water becomes enriched with Fe contents of 2–24,000 μM (Mottl and McConachy, 1990; German and Von Damm, 2004). The hot hydrothermal fluid rises up through the crust and vents at the sea floor. The vent fluid mixes with the oxic deep water and rises up through the water column under its own buoyancy. The plume becomes neutrally buoyant once it is diluted 8,000–10,000 times and the plume density equals that of the surrounding seawater (McDuff, 1995).

In initial studies of mid-ocean ridge axial high temperature, and diffuse low temperature, hydrothermal sites it was estimated that the gross flux of Fe to the ocean was 2.3–19×10^{10} mol y^{-1}, approximately equal in size to the estimated flux from rivers of 2.3×10^{10} mol y^{-1} (Elderfield and Schultz, 1996). The net input of hydrothermal Fe to deep waters, however, was considered to be negligible due to Fe oxide and Fe sulphide mineral precipitation close to the vents (Elderfield and Schultz, 1996; Mottl and McConachy, 1990).

Where substantial sulphide exists relative to Fe in the vent fluid (low Fe/H$_2$S), Fe sulphides precipitate as the buoyant fluids cool and mix with seawater. During this buoyant plume rise dFe remaining in the plume undergoes further mixing with entrained oxic seawater and Fe(II) is oxidised to form Fe(III)-bearing oxyhydroxide precipitates (Mottl and McConachy, 1990). On the other hand, where low sulphide concentrations exist in the vent fluid (high Fe/H$_2$S), such as in ultramafic geological settings, there is little Fe sulphide formation and Fe precipitates principally as Fe oxyhydroxides (Douville et al., 2002). The end mem-

ber vent fluid Fe/H$_2$S is therefore responsible for dictating the extent that Fe precipitates as Fe-sulphides in plumes emanating from vents with different geological settings.

The rate that Fe(II) is oxidised to Fe(III) is an important control on particulate Fe oxyhydroxide formation and hence the concentration of dFe in the hydrothermal plume. The pseudo first order oxidation half-life of Fe(II) varies with changes in oxygen and pH between deep ocean basins from 2.1 min in the relatively oxygenated high pH Atlantic to 6 h in the lower oxygen levels and lower pH observed in the Pacific (Millero et al., 1987; Field and Sherrell, 2000). Therefore the balance between the precipitation of hydrothermal dFe as Fe-oxyhydroxides and Fe-sulphides in plumes is controlled by regional variations in Fe(II) oxidation rate and geological variations in Fe/H$_2$S of vent fluids.

Adsorption onto particulates and uptake by microorganisms will also remove dFe from the plume to ocean sediments (Toner et al., 2009; Li et al., 2014; German et al., 2015). The influence of these processes on plume dFe concentrations is yet to be quantified but is likely to be negligible in comparison to dFe removal by Fe sulphide and Fe oxyhydroxide formation (Rouxel et al., 2016).

Iron sulphide minerals have been identified as colloidal constituents within the dissolved phase of some vent fluids (Yucel et al., 2011; Sands et al., 2012), while in other studies, the complexation of Fe with dissolved organic ligands has also been reported in hydrothermal plumes (Bennett et al., 2008; Hawkes et al., 2013; Kleint et al., 2016). In many cases, Fe-rich colloids are seen to be transported many hundreds to thousands of kilometres from their hydrothermal source (Klunder et al., 2011, 2012; Wu et al., 2011a; Nishioka et al., 2013; Fitzsimmons et al., 2014; Resing et al., 2015).

1.2. Fe isotopes in hydrothermal vents and plumes

Natural variations in stable iron isotope compositions are caused by biological and abiotic redox processes with either kinetic or equilibrium fractionation effects (Welch et al., 2003; Johnson et al., 2004; Anbar et al., 2005). If hydrothermal sources of dFe to the ocean have a distinct δ^{56}Fe signature, they could be used to constrain isotope mass-balance quantifications of Fe sources to the ocean (Conway and John, 2014) or help to reconstruct past oceanic Fe cycles (Horner et al., 2015). However, this utility requires a fully resolved knowledge of the biogeochemical processes that fractionate Fe isotopes as they transition between hydrothermal vents and the open ocean. Furthermore, understanding the fractionation of Fe isotopes in hydrothermal plumes is key to constraining how regional differences in vent and ocean chemistry alter the signature of hydrothermal δ^{56}Fe fluxes into different ocean basins.

The Fe isotope composition of hydrothermal vent fluids is not uniform and several studies report a range from $-0.69 \pm 0.16‰$ to $-0.13 \pm 0.06‰$ (2 SD) (Sharma et al., 2001; Beard et al., 2003; Severmann et al., 2004; Rouxel et al., 2008; Bennett et al., 2009). So far, the fractionation of Fe isotopes in hydrothermal plume particles has been examined in detail by three studies (Severmann et al.,

2004; Bennett et al., 2009; Rouxel et al., 2016) and as part of basin scale studies (Conway and John, 2014; Revels et al., 2015). In all cases, the particulate Fe (pFe) fraction (>0.4 μm) collected on filters was measured and showed that the Fe isotope composition of dFe from the vent source is likely to be modified in the hydrothermal plume by precipitation of Fe oxyhydroxide and/or Fe sulphide mineral particles (Severmann et al., 2004; Bennett et al., 2009; Rouxel et al., 2016). All the work done so far measuring hydrothermal δ^{56}pFe indicates that FeS_2 particles are isotopically light and Fe-oxyhydroxides are isotopically heavy relative to vent fluids. This is coherent with experimental studies that show kinetic isotope fractionation of light Fe isotopes with Fe-sulphide (Butler et al., 2005) precipitation and equilibrium fractionation between Fe (II) and Fe (III) enriching Fe oxyhydroxides in heavier isotopes (Bullen et al., 2001). The influence of these processes on the δ^{56}Fe composition of dFe (δ^{56}dFe) in hydrothermal plumes has not yet been directly measured. Severmann et al. (2004) sampled the sediments, vent fluid and plume particles derived from the Rainbow hydrothermal vent on the Mid-Atlantic Ridge. Neutrally buoyant plume (NBP) particles collected *in-situ* had an average Fe isotope composition (δ^{56}pFe = -0.09 ± 0.03‰ relative to IRMM-14) similar to the surrounding Fe-Mn rich sediments (δ^{56}Fe = -0.11 ± 0.10‰) and the hydrothermal vent fluid (δ^{56}dFe = -0.14 ± 0.02‰). Only the Fe isotope composition of samples collected in the buoyant plume varied significantly at this site, where δ^{56}pFe ranged from +0.24‰ to +1.29‰. Due to its ultramafic host rock the Rainbow vent fluids contain abundant Fe and a very high Fe/H_2S ratio (Douville et al., 2002). Consequently, they precipitate almost exclusively as Fe oxyhydroxides in the plume, with no more than 4% of Fe forming sulphide minerals (Severmann et al., 2004). Therefore the Fe isotope signature of the vent fluid is preserved in the NBP by the near quantitative conversion of vent fluid Fe to Fe oxyhydroxide particles, and the isotopically heavy buoyant plume particles result from partial oxidation of vent fluid Fe(II) (Severmann et al., 2004). The high Fe/H_2S ratio at Rainbow makes this site unusual in comparison to the more widespread basalt hosted hydrothermal vents, where vent fluids have more sulphide relative to Fe, and as much as half of Fe from the vent fluid may form Fe sulphide minerals (Rudnicki and Elderfield, 1993).

Bennett et al. (2009) sampled buoyant plume particles and vent fluids from basalt-hosted hydrothermal vents in the South Atlantic and revealed contrasting results to Severmann et al. (2004). Particles in the buoyant plume appeared isotopically lighter (-0.31 ± 0.06‰ to -0.70 ± 0.14‰, 2SD) than the vent fluids (-0.29 ± 0.05‰, 2SD), which the authors attributed to the influence of Fe sulphide precipitation. This is in agreement with recent work on particles settling out of plumes over the East Pacific Rise where a narrow range of δ^{56}pFe values were observed (-0.43 ± 0.08‰ to -0.68 ± 0.03‰, 2SD) with 42–86% of the Fe was FeS_2 (Rouxel et al., 2016). Using isotope mass-balance, both Bennett et al. (2009) and Rouxel et al. (2016) reasoned the dissolved Fe fraction of the hydrothermal plume would be isotopically heavier than

the vent fluid, but its isotope composition was never measured. Given that a large fraction of vent fluid Fe precipitates as Fe sulphide and Fe oxyhydroxide mineral particles the balance between these two processes in hydrothermal plumes will dictate δ^{56}dFe along with any fractionation from particle adsorption, ligand stabilisation of dFe and the presence of nanoparticles.

The aim of this study is to determine the effective isotope composition of dissolved Fe that is dispersed into the deep-ocean interior from a hydrothermal vent source, and to resolve the mechanisms responsible for isotope fractionation between dissolved and particulate phases during plume mixing and dispersal. Samples were collected from a hydrothermal site in the East Scotia Sea to determine the concentrations of Fe and Mn in the Total Dissolvable (TD), dissolved (d) and particulate (p) size fractions as well as the Fe isotope composition of TDFe and dFe. We provide new constraints on the nature of plume particle interactions and the impact on the deep ocean, which have implications for Fe isotopic mass-balance studies of the present and past oceans.

2. MATERIALS AND METHODS

2.1. Study areas

The East Scotia Ridge (ESR) is located in the Southern Ocean sector of the South Atlantic, southeast of South Georgia and west of the South Sandwich Island Arc (Fig. 1). The ESR separates the Scotia Plate and Sandwich Plate and is a back arc spreading centre. Spreading at the ESR has been occurring for a minimum of 9 Ma and currently proceeds at an intermediate rate of 65–70 mm yr^{-1} (Bruguier and Livermore, 2001). The ridge is split into nine spreading segments, E1–E9. The E2 and E9 segments are topographically distinct from the E3–E8 segments and evidence from seismic reflection shows that E2 and E9 are or have been in the past underlain by axial magma chambers (Bruguier and Livermore, 2001). Hydrothermal plume signals indicative of seafloor hydrothermal venting were initially detected over the E2 segment in 1999 (German et al., 2000). High temperature black smoker chimneys have now been observed and sampled at E2 where the plume signals were first observed (Rogers et al., 2012).

The E2 site is located at 56.089°S, 30.317°W (Fig. 1). Buoyant plume (BP) and vent fluid samples were collected at the Dog's Head site located at a water depth of 2600 m. Dog's Head is a group of three 10 m tall chimneys spaced 1–2 m apart, actively venting hydrothermal fluids at temperatures up to 351 °C, which form the characteristic "black smoke" upon mixing with seawater (Rogers et al., 2012; James et al., 2014). Cooler water from depth is entrained up to the height of neutral buoyancy (~2360 mbsl) in the Scotia Sea (German et al., 2000). Deep waters at this site are Weddell Sea Deep Water partially mixed with Lower Circumpolar Deep water (Naveira Garabato et al., 2002; Hawkes et al., 2013). With no local topographic features to confine the plume, the direction of plume dispersal is controlled by ambient deep water currents (German et al., 2000; Walter et al., 2000; Hawkes
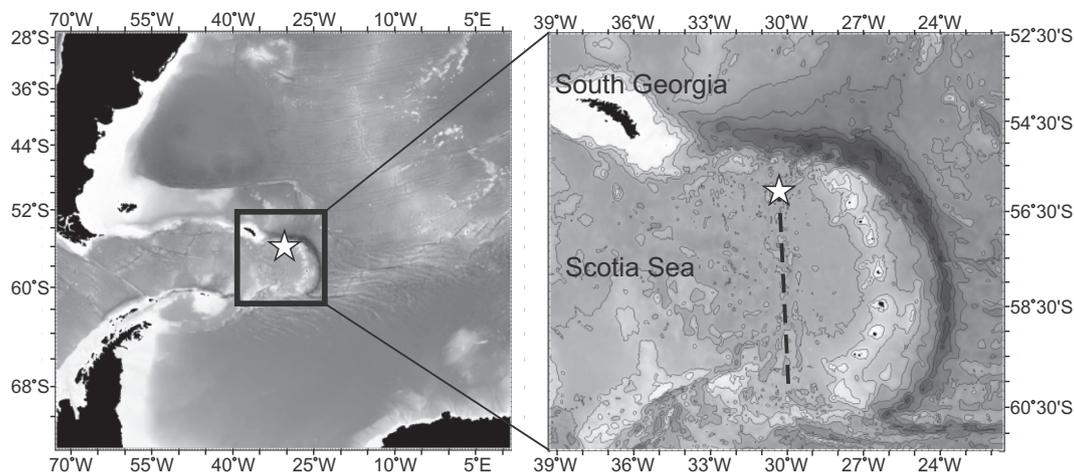
Fig. 1. Study map showing the location of the E2 vent field (star). The dashed line represents the approximate location of the East Scotia Ridge.

et al., 2013), which at the time of sampling transported the plume in an easterly direction.

2.2. Hydrothermal plume detection and sampling

Seawater samples from the BP were collected, filtered and acidified on the RRS *James Cook* during expedition JC080 in 2012. Samples were analysed for trace metal concentrations and Fe isotopes at the National Oceanography Centre in Southampton. The pH and oxygen concentration of several samples were measured on board the ship.

Detection and sampling of the hydrothermal plumes was conducted using a Seabird +911 conductivity, temperature and depth (CTD) profiler system that was attached to a titanium frame that holds 24 externally sprung 10 litre OTE (Ocean Test Equipment) water sampling bottles. These bottles were cleaned at the start of the cruise by filling each bottle with freshwater and an aliquot of HCl. The Niskin bottles are Teflon lined with Teflon taps and non-metallic parts to prevent any contamination during sampling of waters with low concentrations of trace metals. A light scattering sensor (LSS), Eh detector and Stand Alone Pumping System (SAPS) were also mounted on the titanium frame.

The hydrothermal plume was located using the CTD profiler, LSS and Eh detectors to look for deviations in temperature, particulates, and Eh from background seawater. The buoyant part of the hydrothermal plume (BP) was identified by negative Eh anomalies and positive temperature and LSS anomalies. The NBP was detected by positive LSS anomalies and negative Eh and temperature anomalies. These anomalies were evidenced by relative changes in sensor signals in real time whilst towing the CTD rosette across the vent field and simultaneously profiling the water-column (so-termed 'tow-yoing').

During JC80 vent fluid samples were taken from the chimney orifices using the Remotely Operated Vehicle (ROV) *Isis* manipulating a set of titanium syringes (Von Damm et al., 1985) with a temperature probe attached. The probe was aligned with the snorkel of the syringe for simultaneously measuring fluid temperature during sampling. The temperature probe measured temperatures of 320–343 °C during sampling of Dog's Head vents. Vents were sampled at the end of dives to minimise the time between sampling and recovery on deck. This was in order to avoid precipitation of particles within the vent fluid sample during recovery.

Six 1.2 L Niskin bottles were attached to the *Isis* for sampling the buoyant plume. *Isis* was manoeuvred until the black smoke from the vent was observed flowing through the bottles on a camera pointed at the Niskin rosette. Once the black smoke was observed the temperature was recorded using the CTD on *Isis* and the bottles were closed.

2.3. Sample filtration and preservation

All bottles used for sampling were low-density polyethylene (LDPE) and pre-cleaned using the following procedure: 2 days soaked in 2% Decon 90; rinsed 3 times with deionised water (Milli-Q, Millipore, >18.2 MΩ cm); 1 week soaked in 6 M HCl; rinsed 3 times with deionised water; 1 week soaked in 8 M HNO_3; transferred to Class 1000 clean laboratory and rinsed 3 times with deionised water; filled with 0.015 M Teflon distilled HNO_3. Concentrated Teflon-distilled acids were prepared using a Picotrace 'Cupola' sub-boiling (S.B) system. Filters, Teflon filter housings and sampling tubes were soaked in 1.6 M HNO_3 for at least 5 days before being moved to a bath of deionised water where they were stored until required. Filter housings used for samples from the 1.2 L Niskin bottles on *Isis* were cleaned in a separate 1.6 M HNO_3 bath and rinsed 3 times with deionised water prior to use.

Before sub-sampling, Niskin bottles were shaken to homogenize fluid and particles. Samples were transferred from the Niskin bottles under 0.5 bar of pressure using oxygen free nitrogen. 125 ml of unfiltered water sample was sub-sampled from each Niskin for Total Dissolvable (TD) metals. Polycarbonate membrane filters (0.2 μm, Whatman) were used to filter 125 ml of water from Niskin bottles to

collect the dissolved metal size fraction for trace metal analysis. Clean sample bottles were rinsed 3 times with de-ionised water then rinsed with an aliquot of sample water before filling.

Vent fluid samples were transferred and filtered (0.2 μm, Whatman) directly from titanium syringes (Von Damm et al., 1985) to pre-cleaned LDPE bottles for trace metal analysis.

All samples for trace metal analysis were acidified at the end of the cruise using 1 μl of ultra-pure conc. HNO_3 (ROMIL UpA) per 1 ml of sample to achieve a pH < 2, and stored for a minimum of 6 months prior to analysis. This was in order to allow any Fe present as particulates to dissolve in unfiltered TD samples. A comparison of pFe calculated from the difference between TDFe and dFe to the pFe concentration obtained from acid digestion of filters (see next section) showed that TDFe-dFe can account for $99 \pm 38\%$ ($n = 15$) of pFe concentrations. Co-variance of TDFe with REE that adsorb to Fe-oxyhydroxides shows that acidifying with HNO_3 likely dissolves Fe-oxyhydroxides (Lemaitre et al., 2014). The significant difference in Fe concentration between vent samples acidified with HCl and HNO_3 has also been used to infer the presence of FeS_2 nanoparticles (Gartman et al., 2014), which is evidence that at-least partial dissolution of FeS_2 is achieved by acidifying with HNO_3. Therefore our TDFe samples are reasoned to reflect all dFe, the majority of Fe oxyhydroxides, Fe sulphides and biogenic Fe along with any Fe adsorbed to particles, be they lithogenic, authigenic or biogenic.

2.4. Determination of trace metal concentrations in plume samples

Concentration measurements of dissolved and Total Dissolvable metals followed a three step procedure: (1) diluting samples to evaluate the range of concentrations sampled, (2) identifying any samples from step (1) with concentrations below the limit of detection (l.o.d) or with a high blank contribution for pre-concentration and re-analysis, (3) repeat analyses of Fe concentration by isotope dilution – a useful by-product of Fe isotope analyses by double spike (Lacan et al., 2010; Conway et al., 2013).

Initially samples were diluted 21-fold in 1 M S.B. HNO_3. Several samples were doped with a Mn and Fe standard to determine concentrations by standard addition. Dilute sample-spike solutions were analysed using an Element 2 (Thermo Scientific) Inductively Coupled Plasma-Mass Spectrometer (ICP-MS). Procedural blanks for Fe and Mn calculated from the analysis of 1 M S.B. HNO_3 were 1 and 0.2 nmol kg^{-1} respectively, with corresponding instrument limits of detection (3σ of blanks, $n = 15$) of 0.5 and 0.2 nmol kg^{-1}. Two reference materials were analysed to assess accuracy. The measured Fe and Mn content of SLRS-4 (National Research Council, Canada) was 1812 $\pm$ 49 nmol kg^{-1} Fe and 66 $\pm$ 5 nmol kg^{-1} Mn ($n = 8$), which compares well to certified values of 1844 $\pm$ 90 nmol kg^{-1} Fe and 61.3 $\pm$ 0.2 nmol kg^{-1} Mn. Good agreement was also demonstrated at lower concentrations; measured values of Fe and Mn (14 $\pm$ 10 nmol kg^{-1} and

48 ± 3 nmol kg^{-1}, $n = 8$) in CASS-4 (National Research Council, Canada) compare well to certified values (12 $\pm$ 1, 50.60 ± 0.34 nmol kg^{-1} respectively).

Samples with measured Fe concentrations <400 nmol kg^{-1} (i.e. where the blank contribution was >10%) were re-analysed by pre-concentration (Milne et al., 2010; Biller and Bruland, 2012) onto a chelating resin that uses carboxymethylated pentaethylenehexamine (CM-PEHA resin) (Kagaya et al., 2009). Fe concentrations determined for CASS-4 (11.1 $\pm$ 0.5 nmol kg^{-1}, $n = 3$) and NASS-6 (9.0 $\pm$ 0.7 nmol kg^{-1}, $n = 6$) had excellent agreement with their certified values (12 $\pm$ 1 nmol kg^{-1} and 8.6 $\pm$ 0.8 nmol kg^{-1}, respectively), with a corresponding Fe blank of 0.2 nmol kg^{-1} and limit of detection (3σ of blanks, $n = 6$) of 0.1 nmol kg^{-1}.

Initial ICP-MS determinations of TDFe and dFe in diluted and pre-concentrated samples were used to estimate the volume required for $\sim$200 ng of Fe used in the isotope analysis described below. The reported sample concentrations of dFe and TDFe were determined by isotope dilution using Multi-Collector (MC) ICP-MS, as has been used elsewhere (Lacan et al., 2010; Conway and John, 2014). For accurate determination of concentrations, the double spike Fe isotope composition was calibrated by inverse deconvolution of a 3.6 μmol kg^{-1} spike-reference material (IRMM 14) mix with Fe concentration determined by inverse isotope dilution of a spike-certified Fe standard mix (Inorganic Ventures) of known concentration with a relative standard deviation (RSD) of $\pm$0.3%. The maximum RSD on repeat Fe measurements by double spike MC-ICP-MS was $\pm$0.1% ($n = 2$), and is an improvement on the precision of Fe concentrations initially measured by ICP-MS where the RSD was up to $\pm$6% ($n = 17$). The accuracy of Fe measurements by MC-ICP-MS was assessed by inter-comparison with the previous measurements by ICP-MS and all values agreed within 11% ($n = 38$). Subsequently Fe concentration data reported herein were determined by MC-ICP-MS because it provides sufficient accuracy with the best precision available. All sample and spike volumes were weighed on a balance with repeatability down to 0.001 g and we therefore assume that the weighing error is insignificant relative to the instrument error.

Particles collected from 0.6 to 3 L of sample passed through 0.2 μm filters were dissolved in concentrated nitric acid at 150 °C for 3 days following the method of German et al. (1991). Dissolution efficiency was assessed using the RTS-1 sulphide ore mill tailings reference material. This reference material was deemed the most likely to have similar Fe mineralogy to hydrothermal plume particles in comparison to other reference materials. Recoveries of Fe, Zn and Cu from a weighed amount of RTS-1 were 94 $\pm$ 2%, 126 $\pm$ 9% and 110 $\pm$ 10%. Particles collected on SAPS filters were also characterised using scanning electron microscope energy dispersive X-ray (SEM-EDX) as described in the Supplementary Information.

Concentrations of dCu, dZn, dV, and dMg in the vent fluid samples were measured by dilution in 0.3 M S.B. HNO_3 and analysis on a X-Series 2 quadrupole ICP-MS (Thermo Scientific). Vent fluid concentrations of dFe and dMn were diluted in the same way but measured by ICP

Atomic Emission Spectroscopy (AES) (Thermo Scientific iCAP 6000 Plus Series). The concentration of chloride in the vent fluids was measured by ion chromatography (IC; Dionex ICS2500).

Oxygen concentration and alkalinity were measured at sea as soon as possible after sampling. Oxygen was measured using the Winkler Titration (Hansen, 2007) with a standardised iodate solution (1.667 mM) (OSIL) and alkalinity by the Gran titration method (Kaeding, 1973).

2.5. Fe isotope analysis

The iron isotope composition of samples was determined using a ^{57}Fe and ^{58}Fe double spike method adapted from Lacan et al. (2010). All sample handling was carried out under laminar flow hoods, set within a Class 1000 clean laboratory to minimise the potential for airborne sample contamination.

Initial matrix removal and pre-concentration of spiked samples was carried out using nitriloacetic acid (NTA Superflow, Quiagen) resin packed into a $\sim$5 cm^3 volume of a 12 cm long handmade column constructed from Perfluoroalkoxy alkane (PFA) tubing with the resin retained by Teflon frits with 20 μm pores. Samples were prepared by acidifying to a pH between 1.7 and 1.8 several days before adding the double spike in equi-molar concentration to the sample. After adding the double spike, 1 μl of 0.1 M H_2O_2 (Upa ROMIL) was added per 1 ml of sample 1 h prior to loading the sample onto the NTA columns. Prior to sample loading, NTA columns were cleaned using 75 ml 1.5 M S.B. HCl and 80 ml de-ionised water (18.2 MΩ cm, Milli-Q) checking that the pH was neutral after the de-ionised water rinse. Samples were loaded onto the columns and rinsed with 80 ml de-ionised water to remove salts. Iron was then eluted from the NTA columns using 10 ml of 1.5 M S.B. HCl. The eluate was collected in 15 ml PFA vials (Savillex), dried down and reconstituted in 0.5 ml 6 M S.B. HCl + 0.001% v/v H_2O_2, in preparation for a secondary purification step.

AG1-X8 anion-exchange resin with 100–200 dry mesh size (Bio Rad) was used to further purify Fe in the samples. Handmade polyethylene columns ($\sim$9 cm length and $\sim$0.4 mm diameter) were filled with the AG1-X8 resin and pre-cleaned once with 5 ml of 0.1 M ultrapure HF; four times filling the columns with 6 M S.B. HCl followed by 7 M S.B. HNO$_3$ then with 2 ml of 1 M S.B. HCl (all acids had a concentration of 0.001% v/v H_2O_2). The resin was then conditioned with 1 ml 6 M S.B. HCl + 0.001% v/v H_2O_2 before the sample was loaded onto the columns in 0.5 ml 6 M S.B. HCl + 0.001% v/v H_2O_2 and rinsed using 3.5 ml of 6 M S.B. HCl + 0.001% v/v H_2O_2. Iron was eluted from the resin using 4 mL of 1 M HCl + 0.001% v/v H_2O_2 and collected in a 7 ml Teflon vial. The procedural blank was estimated as 0.9 ± 0.3 ng Fe ($n = 5$) by taking de-ionised water through the entire procedure.

All purified samples were evaporated on a hotplate and re-dissolved in 1–2 ml of 0.3 M S.B. HNO$_3$ for isotopic analysis by MC-ICP-MS (Thermo Fisher Neptune and Neptune Plus with the same configuration) with aluminium skimmer and sample cones. Samples were introduced using an Aridus II (CETAC) or Apex-Q (ESI) desolvator and masses ^{54}Fe, ^{56}Fe, ^{57}Fe, ^{58}Fe, ^{53}Cr and ^{60}Ni were measured. There was no difference in data quality from these different introduction systems. Fe concentrations for isotope analysis were 200 ng/ml introduced at 75 μl min^{-1} using a PFA nebuliser. Analysis by MC-ICP-MS was conducted in 'high-resolution' mode using a high-resolution slit in order to resolve polyatomic interferences on ^{54}Fe, ^{56}Fe and ^{57}Fe. Sample analysis consisted of 50 repeat measurements of 4.2 s. A blank (the same 0.3 M S.B HNO$_3$ samples were dissolved in) solution was measured before and after every sample/standard, with 20 repeat measurements of 4.2 s. Sample and blank uptake time was 80 s. Wash time before each sample/standard was 60 s. The wash time before blanks was 300 s when using the Apex-Q and increased to 900 s when using the Aridus. The instrument was tuned until the mass resolution was >8000 with a plateau >200 ppm. The centre mass for measurements was 2/5ths along the length of the signal plateau and a sequence of standards were analysed before measuring any samples in order to assess instrument performance. Isotopes ^{53}Cr and ^{60}Ni were monitored in order to correct for any isobaric interferences from ^{54}Cr on ^{54}Fe and ^{58}Ni on ^{58}Fe. Detectors measuring ^{53}Cr and ^{60}Ni used 10^{12} Ω resistors to improve the accuracy of low intensities from these isotopes. All other detectors used 10^{11} Ω resistors. Sequences were set up on the instrument with a standard bracketing approach in the repeating order reference material (IRMM), internal standard (ETH), Sample 1, Sample 2, with all solutions being a mix of sample/standard plus the double spike. The mean beam intensity of blanks bracketing each sample/standard is subtracted from the sample/standard analysis. Mass bias on sample/standard measurements is corrected for by iteratively deconvolving the spike-sample mix following the data reduction methodology of Bonnand et al. (2011). ^{54}Cr and ^{58}Ni interferences were corrected based on beam intensity (Albarede and Beard, 2004). This correction procedure assumes instrumental mass bias is the same for Fe, Cr and Ni with $^{53}Cr/^{54}Cr$ and $^{58}Ni/^{60}Ni$ equal to natural abundances (Dauphas et al., 2009). Instrument accuracy was assessed by repeat measurements of IRMM-14 and Eidgenössische Technische Hochschule (ETH) Zürich standards. The precision of Fe isotope measurements was ±0.07‰, 2 SD, based on repeat analysis of IRMM-14 (0.00 ± 0.07, 2SD, $n = 40$), samples (mean error ± 0.07, 2SD, from 2 repeats of $n = 11$ samples) and ETH standard (0.51 ± 0.07, 2SD, $n = 32$). To assess accuracy and precision of the entire method de-ionised water doped with the ETH standard and taken through the full procedure gave values of 0.52 ± 0.10 (2SD, $n = 5$). Both instrument and method analyses of the ETH standard were in agreement with the consensus value of 0.53 ± 0.06 (2SD, $n = 6$) (Levasseur et al., 2004; Poitrasson and Freydier, 2005; Teutsch et al., 2005; Lacan et al., 2008, 2010).

All isotope values reported here are in delta notation relative to the standard reference material IRMM-14:

$$\delta^{56}Fe(\text{‰}) = ((^{54}Fe/^{56}Fe)_{sample}/(^{54}Fe/^{56}Fe)_{IRMM-14} - 1) \times 1000$$

$$(1)$$

3. RESULTS

3.1. Vent fluid composition

The mean temperature of vent fluids issuing from several different chimneys was 333 °C, which is typical of black smoker type hydrothermal vents (Table 1) (Ishibashi, 1995). Measured chloride concentrations were slightly higher than background seawater (540 mM), which is typical of vents in back arc basins (Gamo et al., 2006). A vent fluid Mg content of 0.9–1.6 mM was highly depleted relative to a Scotia Sea bottom water concentration of 53.5 mM (James et al., 2014), and showed that only a negligible proportion of background seawater (1.9–3.1%) was entrained with the vent fluid during sampling.

Concentrations of dFe, dMn, dCu, dZn and dV in the vent fluids were similar in all samples, with relative standard deviations (RSD) typically <8% of mean values. The RSD of Mg concentrations across all samples was higher (18%), but still only reflects minor seawater entrainments up to 3.1%, which result in negligible differences between observed values and predicted mean end-member element concentrations (Table 1).

Hydrothermal end-member Fe and Mn concentrations of the 1.4–2.0 mM are relatively high compared to the global range measured for back arc basin vents of 0.4–6.8 mM for Mn and 0.02–1.7 mM for Fe (Ishibashi, 1995), but comparable to end-member vent fluid concentrations reported previously for this site (James et al., 2014). The end-member Cu concentration we observed (0.0396 mM) were also at the high end of previously reported values from vents in a back arc basin, which vary from 3×10^{-6} to 0.034 mM (Ishibashi, 1995). Whereas Zn concentrations of 0.282 mM were intermediate in this respect, compared to values between 7×10^{-3} and 7 mM (Ishibashi, 1995). Both Cu and Zn are approximately double the end-member values calculated previously of 0.146 mM and 0.0185 mM (James et al., 2014) indicating an increase of Zn and Cu in the three years between sampling.

The end-member molar ratio of chalcophile elements to Fe in the vent fluids was 0.028 for Cu/Fe and 0.201 for Zn/Fe. In comparison to previous Fe isotope studies from hydrothermal vents, the Cu/Fe and Zn/Fe ratios at Dog's Head were higher than at Red Lion in the South Atlantic, which had ratios of <0.01 for Cu/Fe and 0.13 for Zn/Fe

(Bennett et al., 2009). The ratios from Dog's Head were also much higher than those reported from Rainbow, in the North Atlantic, which were <0.01 for Cu/Fe and <0.01 for Zn/Fe (Douville et al., 2002).

Herein we consider the plume sample with a dMn maxima of 11.2 µmol kg^{-1} collected directly above Dog's Head chimney (5 m) to be representative of the end-member vent-fluid. Our assumption of TDFe conservation within 5 m of buoyant plume rise is supported by the in situ observations that particles do not attain settleable size within the immediate plume over the vent orifice (Cotte et al., 2015; Estapa et al., 2015). Further, the δ^{56}TDFe of the plume sample that we assume to equate to the vent fluid had an Fe isotope composition of -0.31 ± 0.03‰ (Fig. 6b), which is centred within the range of δ^{56}Fe values reported previously for vent fluids sampled from other sites of -0.69‰ to -0.13‰ (Sharma et al., 2001; Beard et al., 2003; Severmann et al., 2004; Rouxel et al., 2008; Bennett et al., 2009).

3.2. Buoyant plume detection

Negative anomalies in Eh and positive anomalies in temperature and LSS at a depth of 2600 m indicated that the buoyant plume was sampled by the CTD rosette very close to if not directly over the Dog's Head chimney, which is located at 2600 m depth (Fig. 2).

The influence of other nearby venting edifices from E2 can be ruled out as they are not known to generate significant particulate plumes (James et al., 2014).

3.3. Fe and Mn concentrations in the buoyant plume

Dissolved Mn (dMn) has been used as a near-conservative tracer of plume dilution in previous plume studies (James and Elderfield, 1996; Field and Sherrell, 2000), as the oxidation rates of reduced Mn are considered to be negligible compared to the time scales of plume dispersal at our study site (Cowen et al., 1990). The TDFe, dFe and dMn content of the buoyant plume was 2–3 orders of magnitude higher than background Scotia Seawater (Fe and Mn = 0.4 and 2.8 nM) (Loscher et al., 1997; Klunder et al., 2011; Hawkes et al., 2013). The concentration of TDFe was 13.6 µmol kg^{-1} in black smoke above the hydrothermal vent and dropped to 0.49 µmol kg^{-1} during

Table 1
Hydrothermal vent fluid composition at E2, Dog's Head. Temp. is the maximum temperature recorded during sampling from a temperature probe attached to the snorkel of the titanium sampler.

| Sample	Temp. (°C)	Cl-(mM)	dFe (mM)	dMn (mM)	dCu (mM)	dZn (mM)	dV (mM)	dMg (mM)
B1-02	343	555	1.41	1.96	0.0420	0.258	0.485	1.51
B1-03	343	556	1.41	1.97	0.0394	0.265	0.543	1.65
B2-08	320	550	1.40	1.99	0.0386	0.268	0.596	1.68
Y1-06	346	558	1.25	2.00	0.0367	0.295	0.611	1.00
Y2-01	324	553	1.37	1.99	0.0370	0.280	0.570	1.25
Y2-04	324	556	1.37	2.03	0.0373	0.280	0.562	1.41
Mean	333	555	1.37	1.99	0.0385	0.274	0.561	1.42
RSD (%)	4%	1%	5%	1%	5%	5%	8%	18%
End-member		555	1.40	2.00	0.0396	0.282	0.577	0
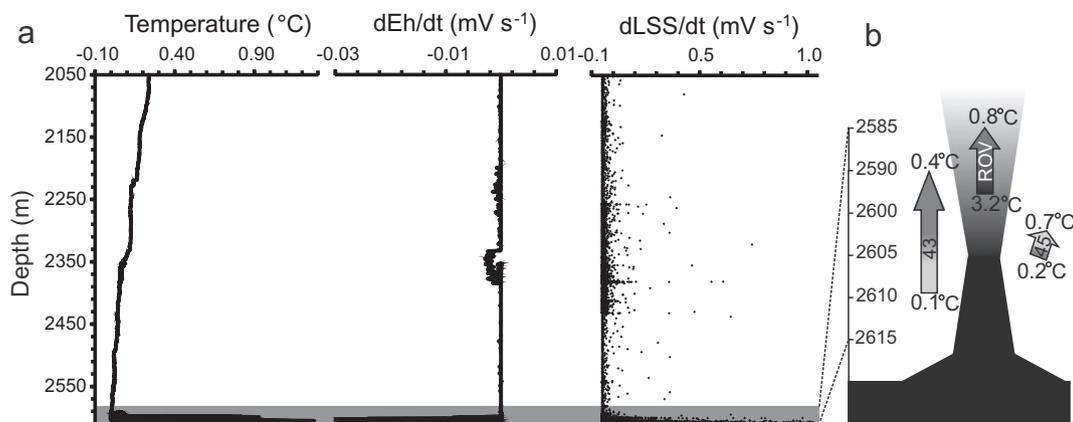
Fig. 2. Tow-yo profile of main sampling cast (CTD 45) showing temperature, delta Eh/ delta time, and delta light scattering signal/ delta time (a). The depth of buoyant plume samples collected for Fe isotope analyses is represented by the grey bar. Further details of sampling are provided by the schematic diagram (b) where arrows represent the path of the sampling equipment relative to depth (m) on the y-axis. Corresponding *in-situ* temperature (°C) range of samples is noted at either end of the arrows. Numbers on arrows correspond to designated CTD cast numbers with ROV representative of samples taken using *Isis* in the black smoke of the plume.

dispersal in the buoyant plume (Fig. 3). These elevated concentrations are further indication that the core of a particle rich hydrothermal plume was sampled and we assume that a negligible fraction of TDFe is derived from lithogenic particles. Similarly to TDFe, dFe concentrations decreased from 9.20 to 0.05 μmol kg^{-1} and were always less than the corresponding TDFe concentration (Fig. 3). Dissolved Mn was 11.2 μmol kg^{-1} in near vent samples, and down to 0.6 μM in more dispersed samples further away from the vents. Dissolved Mn was consistently more abundant than dFe in the buoyant plume, where dFe/dMn ranged from 0.81 in near vent samples down to 0.07 in more distal samples, and was mainly lower than the mean vent fluid ratio of 0.69. The TDFe/dFe ratio ranged from 1.11 to 6.56 in the buoyant plume, with higher ratios in more dispersed samples reflecting a greater proportion of particulate Fe in the TDFe samples.

3.4. Sample aging within Niskin bottles

Metal concentrations in the 'dissolved' and 'Total Dissolvable' fractions represent their partition at the time of filtering rather than in the water column at the time of sampling. In the case of Fe, the formation of pFe from dFe is rapid enough that we must consider the likely artefacts that arise from the delay between sampling and filtering times. Samples were stored in the Niskin bottles for between 2 to 7 h before they were filtered. Samples were filtered in the order that they had been collected, to minimise the storage time before filtration.

Several samples were taken sequentially from two recovered Niskin bottles over a period of 24 h to study the rate of Fe precipitation within the sampling bottles and its influence on δ^{56}dFe (Fig. 4). The measured dFe concentration in both samples decreased significantly over 24 h from
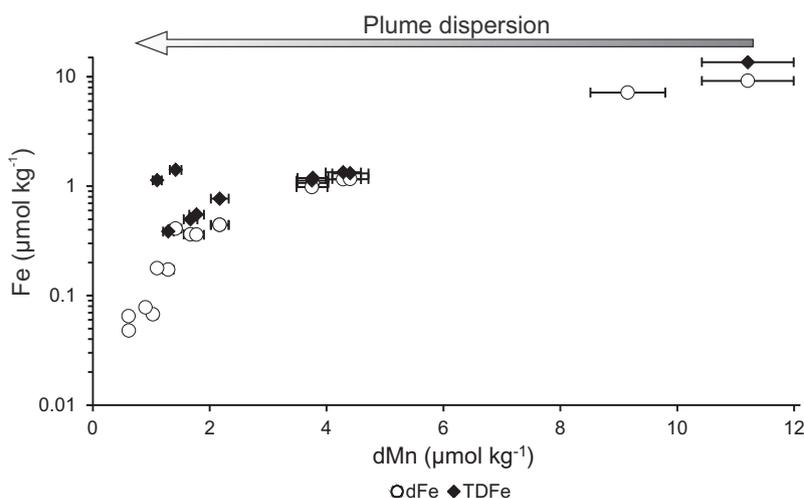

Fig. 3. Concentrations of TDFe (black diamonds) and dFe (open circles) plotted against the near-conservative tracer dMn. Error bars represent 6% RSD error on dMn measurements. Error bars on Fe concentrations are smaller than the size of data point markers.
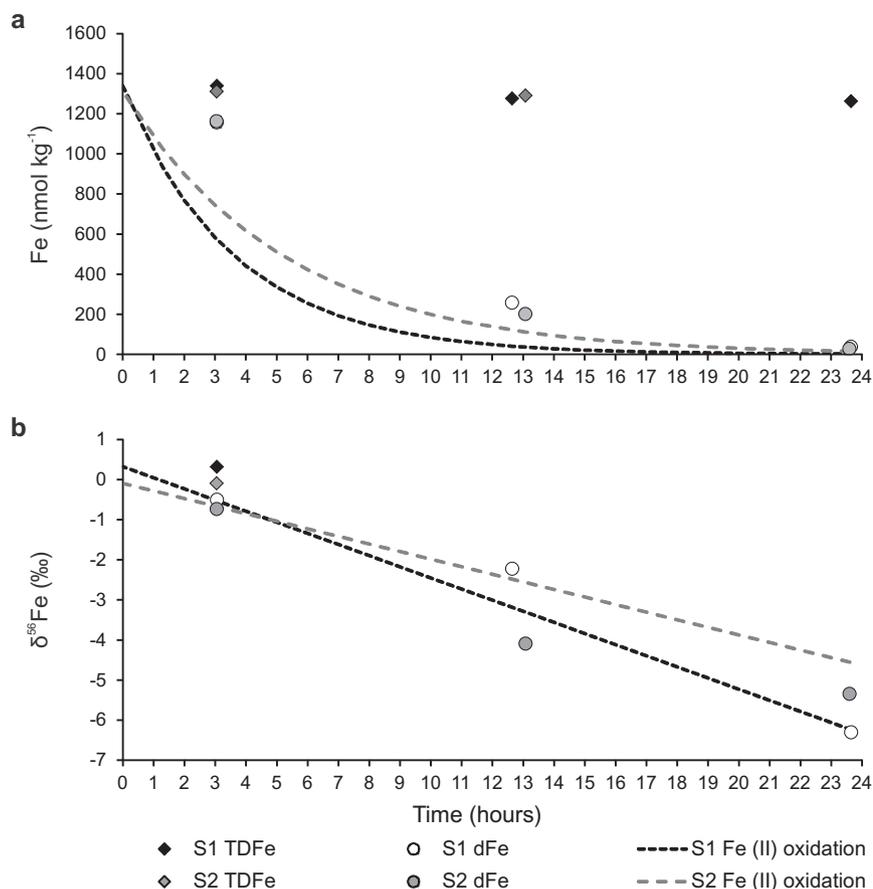
Fig. 4. Observed and predicted behaviour of (a) dFe and TDFe concentration and (b) dFe isotope composition (δ^{56}dFe) for two samples (S1 and S2) sub-sampled intermittently from their Niskin bottles over 24 h. Predicted concentrations (dashed lines) assume dFe is comprised of Fe (II), Fe (II) oxidation half-life is 2.50 (S1) and 3.67 (S2) hrs (Supplementary information, Table S1). It is also assumed that all TDFe was present as dFe at the time of sampling ($t = 0$), so predicted dFe concentrations are a maximum possible estimate. The predicted trends in δ^{56}dFe (dashed lines) assume dFe is comprised of Fe(II) and follows the same oxidation rates using a Rayleigh equation and fractionation factor of 1.0009 between ferrihydrite and Fe$_{(aq)}$ (Bullen et al., 2001).

1160 nM to 27–37 nM, while TDFe concentrations were quasi-stable between 1350 and 1200 nM (Fig. 4a). The stability of TDFe over time confirms only minor loss of TDFe from the system over time. This is likely to be the result of particles becoming trapped in or beneath tap fittings on the Niskin bottle.

Following the approach of Field and Sherrell (2000) and Bennett et al. (2009), the average Fe(II) oxidation half-life in the plume at E2 was calculated to be 3.67 h (supplementary information, Table S1). However, this may range from 1.45 to 5.63 h, if input parameters from background Scotia seawater (Hawkes et al., 2013) or samples taken directly over the vent chimney are used instead. Measured dFe concentrations in the two Niskin bottles were always higher than the Fe(II) concentrations predicted from Fe(II) oxidation kinetics (Fig. 4a), which may result from a partial presence of Fe(III) oxyhydroxide nanoparticles or colloids in the dFe pool. In accord with dFe oxidation to Fe(III), δ^{56}dFe also decreased from $-0.50‰$ and $-0.74 \pm 0.05‰$ to $-6.30 \pm 0.05‰$ and $-5.35 \pm 0.08‰$, compared to δ^{56}TDFe compositions of 0.32‰ and $-0.10 \pm 0.05‰$.

A delay of 2 to 7 h between sampling and filtration corresponds to roughly one to two Fe(II) oxidation half-lives. Despite this, there was little change in Fe/Mn that would be expected if a significant amount of dFe was forming particulate Fe oxyhydroxides within Niskin bottles during sample recovery (supplementary information, Fig. S2). For the purposes of our discussion, we assume that any sample aging within the Niskin bottles is analogous to plume aging in the water column with the caveat that oxidation of Fe in the water column will occur more quickly as plume waters are continuously mixed with oxic seawater. Furthermore the dFe isotope composition can be compared to the mineralogical composition of pFe filtered from the Niskin bottles in order to assess how precipitation of Fe mineral particles influences dFe isotope composition and how this relates to the dFe isotope composition of the *in-situ* plume.

3.5. Hydrothermal particle composition

The mineralogy of hydrothermal particles can be examined indirectly using chalcophile elements that also form

sulphides, and the particle-reactive element vanadium (V), which is sensitive to scavenging by Fe oxyhydroxides. The oxyanion VO_4H^{2-} is co-precipitated and scavenged at constant molar ratios by Fe-oxyhydroxides depending on the local phosphate concentration (Feely et al., 1998) and this relationship can be used to calculate the fraction of pFe present as Fe-oxyhydroxides.

Concentrations of particulate V (pV) and Fe (pFe) were positively correlated in the buoyant plume ($r^2 = 0.955$), for all but two of the highest concentration samples near the vent chimney (Fig. 5a), indicating the widespread occurrence of Fe oxyhydroxides. The outliers in Fig. 5a also contained the highest concentrations of particulate chalcophile elements (Fig. 5b and c), suggesting that these particles contained significant Fe sulphides.

The ratio of pV/pFe in the E2 buoyant plume was 3.0×10^{-5}, and much lower in the sulphide dominated outliers (0.1×10^{-5}). The pV/pFe ratio observed in other Atlantic hydrothermal plumes is highly variable, $1.0–30 \times 10^{-5}$ (Feely et al., 1998; Bennett et al., 2009), whereas similar values ($2.9–3.0 \times 10^{-5}$) are observed over the East Pacific Rise (EPR) and also Juan de Fuca Ridge (JdFR; $2.3–2.8 \times 10^{-5}$) (Feely et al., 1998). Thus the pV/pFe ratios measured in particles over E2 are more similar to plumes from the EPR and JdFR than sites in the Atlantic Ocean, perhaps indicative of the similarity of Fe particle-forming processes between these regions. Alternatively, such similarities could result from the V/Fe ratios in vent fluids from these regions, although variable input of V is not considered to have a significant effect on pV/pFe in the plume

(Trefry and Metz, 1989). Overall the strong correlation between pV/pFe suggests that the formation of Fe-oxyhydroxides is the main Fe particle forming process throughout the rising plume over E2. We observed higher ratios of pCu/pFe and pZn/pFe than previously observed in a hydrothermal plume. The E2 plume has pCu/pFe of $8–14 \times 10^{-2}$, compared to previous observations in the Atlantic and Pacific Oceans of $0.3–8 \times 10^{-2}$ (Feely et al., 1994a; Edmonds and German, 2004; Bennett et al., 2009; German et al., 1996; James and Elderfield, 1996). Particulate Zn was also enriched with respect to pFe at E2, where pZn/pFe was $19–310 \times 10^{-2}$, compared to $0.1–29 \times 10^{-2}$ from Atlantic and Pacific Ocean sites (Feely et al., 1994a; Edmonds and German, 2004; Bennett et al., 2009; German et al., 1991). The abundance of chalcophile elements at E2 means they serve as a particularly sensitive indicator of sulphide precipitation in the near vent region of the buoyant plume to support our interpretation of the Fe particle forming processes during plume mixing and dispersal.

3.6. Fe isotope composition of TDFe and dFe

Dissolved Mn concentrations can be used to trace the dilution of hydrothermal vent fluids by seawater because its behaviour is quasi-conservative on the time-scales of plume rise, except for a minor amount of scavenging to Fe oxyhydroxide particles (Cowen et al., 1990; James and Elderfield, 1996; Field and Sherrell, 2000). In general, as the plume becomes more dispersed (and hence the dMn
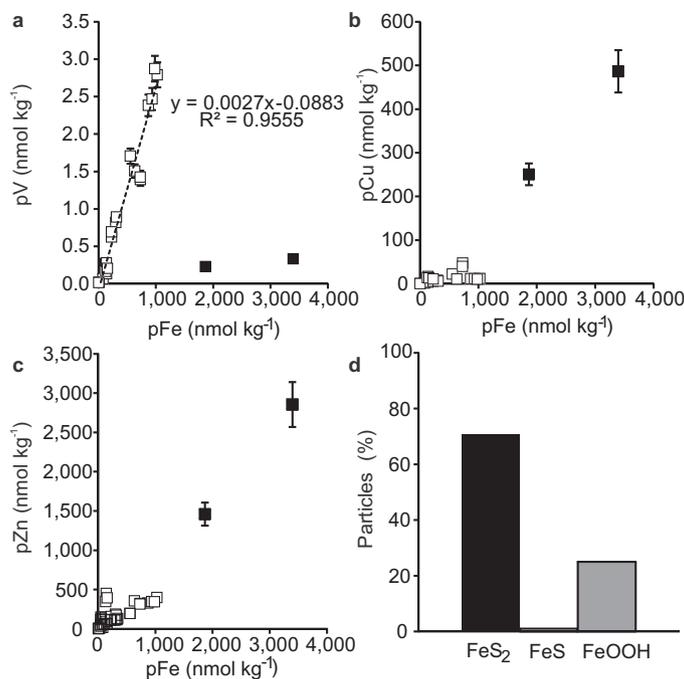

Fig. 5. Concentration of (a) pV, (b) pCu and (c) pZn relative to pFe in the buoyant plume above the E2. Outliers (excluded from the linear regression) are highlighted in black, and are consistent with the presence of Fe sulphide minerals in an otherwise Fe oxyhydroxide dominated hydrothermal plume. Composition of particles ($n = 24$) collected on SAPS filters directly over the vent (similar depth and temperature as black points in a, b and c) show (d) that the main Fe sulphide mineral is pyrite (FeS_2); see Supplementary Information for further details.

concentrations decrease) δ^{56}TDFe values become heavier, with the vent-proximal plume containing δ^{56}TDFe of $-0.31 \pm 0.03‰$ and the more dispersed plume containing δ^{56}TDFe of $0.78 \pm 0.05‰$ (Fig. 6b).

The δ^{56}Fe of dFe (δ^{56}dFe) in plume samples ranged from $-2.39 \pm 0.05‰$ to $-0.13 \pm 0.05‰$, and indicates dFe was enriched with lighter values during plume dilution and dispersal (Fig. 6b). The difference between δ^{56}dFe and δ^{56}TDFe (here after referred to as Δ^{56}Fe$_{d-TD}$) is consistently negative because δ^{56}dFe was always lighter than the corresponding δ^{56}TDFe (Fig. 6b). Δ^{56}Fe$_{d-TD}$ ranged from -0.11 ± 0.04 in the vent-proximal plume to $-2.13 \pm 0.07‰$ in the

dispersed plume (Fig. 6c). Hence the degree that Fe isotopes were fractionated between dFe and TDFe samples was also a function of plume dispersal.

4. DISCUSSION

4.1. Fe(II) oxidation and isotope fractionation in the buoyant plume

The main processes that removes dFe from hydrothermal plumes is the precipitation of Fe-sulphides followed by the oxidation of Fe(II) to Fe(III), where the resultant
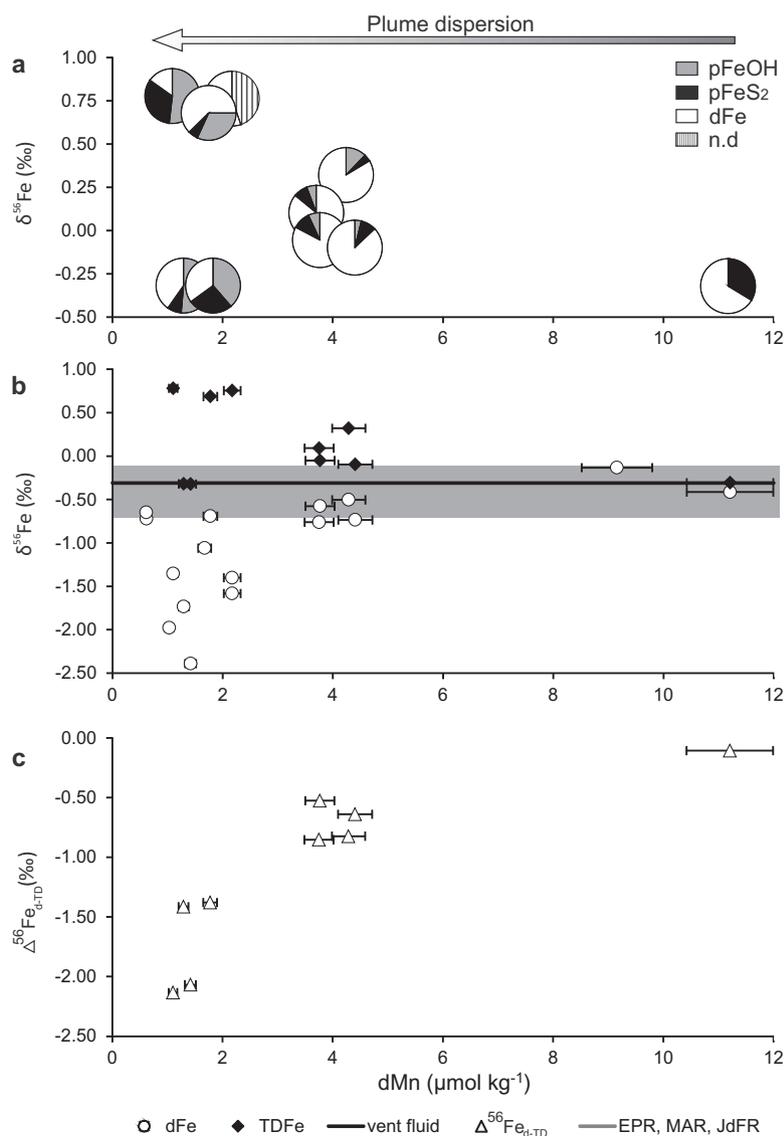

Fig. 6. (a) abundances of dFe (white) pX_{FeS2} (black) and pX_{FeOOH} (grey) within TDFe, vertical lines indicate no data for composition of particle fraction (see Section 4.2 Eqs. (2) and (3)), (b) isotopic composition of dFe and TDFe, (c) difference in isotopic composition of dFe and TDFe (Δ^{56}Fe$_{d-TD}$), as a function of plume dMn, which can be used as a proxy of plume dispersion. Position of pie charts in panel a corresponds to position of TDFe in b. The grey band in panel B represents the range of δ^{56}TDFe values of vent fluids measured in previous studies (Sharma et al., 2001; Beard et al., 2003; Severmann et al., 2004; Rouxel et al., 2008; Bennett et al., 2009). The black line represents the δ^{56}dFe value of the hydrothermal vent source at the Dog's Head chimney on the E2 vent field.

precipitation of Fe sulphides and oxyhydroxides will contribute to the pFe and TDFe phases. Precipitation of Fe-sulphides is the dominant process in the first 10's of metres of plume rise where sulphide concentrations are saturated. As the plume rises 100's of metres sulphide becomes under saturated and Fe oxyhydroxide formation is the dominant mineral precipitation pathway. Redox transformations impart a significant isotopic fractionation to Fe (Bullen et al., 2001), hence the oxidation of dissolved Fe(II) is expected to be a key process controlling the isotope composition of dissolved and particulate Fe fractions in hydrothermal plumes.

The rate of Fe oxyhydroxide formation in a plume is controlled by the production of Fe(III) from Fe(II) supplied from the highly-reducing vent fluids. Fe(III) forms Fe oxyhydroxide colloids (<0.2 μm), which subsequently aggregate to form Fe oxyhydroxide particles (>0.2 μm) that are collected on the filter during filtration (Schwertmann et al., 1999). Experimental and theoretical studies show that oxidation of Fe(II)$_{(aq)}$ favours production of isotopically heavier Fe(III)$_{(aq)}$ (Bullen et al., 2001; Welch et al., 2003; Anbar et al., 2005; Wu et al., 2011b). Precipitation of Fe(III)$_{(aq)}$ as Fe oxyhydroxides also favours the heavier isotopes of Fe via a kinetic isotope fractionation mechanism, which depends on the rate of mineral precipitation (Skulan et al., 2002) and the exchange of Fe on the mineral surface (Icopini et al., 2004; Teutsch et al., 2005; Mikutta et al., 2009). Due to rapid equilibration between Fe(II)$_{(aq)}$ and Fe(III)$_{(aq)}$, within 150–300 s (Welch et al., 2003), and the instability of Fe(III)$_{(aq)}$, we expect the oxidation of Fe(II)$_{(aq)}$ to contribute isotopically heavier Fe oxyhydroxides to the pFe fraction leaving the remaining Fe(II) in the dFe fraction isotopically light.

The assumption of an entirely ferrous and aqueous dFe fraction, however, is a simplification of reality. In the 24 h plume aging experiment, we recorded a slower drop in dFe concentration over time than predicted by the oxidation kinetics of Fe(II) (Fig. 4a). Additionally, the range of oxidation half-lives calculated throughout the plume (supplementary Information, Table S1) is slow compared to previous observations from the Atlantic Ocean, which ranged from 17 to 27 min (Field and Sherrell, 2000), meaning our reported discrepancy between observed and predicted dFe is probably conservative. Clearly, the assumed aqueous Fe(II) oxidation to form particulate Fe oxyhydroxides is unable to fully account for our observed concentrations of dFe.

Recent work has shown that 80% of the dFe in a hydrothermal plume over the MAR was indeed present as Fe(II) (Sedwick et al., 2015), however up to 82–96% of dFe was present as colloids (Fitzsimmons et al., 2015). Previous work on the E2 plume has also shown that 47 ± 26% of Fe is present as colloids and 7.5% of all hydrothermal Fe is stabilised by organic ligands (Hawkes et al., 2013). Therefore, using the Fe(II) oxidation half-life from the bottle experiments we can reason, that Fe(II)$_{(aq)}$ was likely to represent just 50–63% of the initial dFe measured in our bottle experiments (Fig. 4a). We therefore suggest that the dFe comprises of a mixture of aqueous Fe(II), Fe complexed by organic ligands, and colloidal Fe(III) oxyhydroxides.

Nonetheless, we found δ^{56}Fe of dFe in our 24 h bottle experiments to be similar to the Fe isotope composition predicted from the Rayleigh equation and fractionation factors attributable to Fe oxyhydroxide formation after Bullen et al. (2001) (Fig. 4b). A good fit to the Rayleigh equations indicates any Fe sulphide nanoparticles or organic ligands present in the dFe pool were apparently of little significance for shifting the isotopic composition of dFe in the early plume samples used in these experiments at E2.

4.2. TDFe isotope composition and FeS$_2$ precipitation in the buoyant plume

Values of δ^{56}TDFe represent the mass balance of both dissolvable particles and dissolved fractions in the water column. Therefore, δ^{56}TDFe is insensitive to internal isotope fractionations between dFe and pFe pools, unless one of these pools is physically separated from the other. In this instance, δ^{56}TDFe will reflect the revised isotopic composition of its modified mass. Physical mixing processes in the plume are capable of inducing changes to δ^{56}TDFe, e.g., loss of pFe from the buoyant plume by particle aggregation and gravitational settling or more complex dispersion of particles according to their densities within the buoyant plume. A loss of isotopically light pFe from the buoyant plume is required to explain our observed values of δ^{56}TDFe, which become isotopically heavier relative to the plume source during dispersal (Fig. 6b). Iron oxidation does not explain the Fe isotopic trends, but low temperature experimental studies demonstrate there is a kinetic isotope fractionation during Fe sulphide precipitation, which favours reaction with lighter Fe isotopes (Butler et al., 2005; Polyakov et al., 2007; Rouxel et al., 2008), and produces isotopically light Fe sulphide particles. Large (>20 μm) Fe sulphide aggregates (Mottl and McConachy, 1990; Feely et al., 1994c; Yucel et al., 2011; Carazzo et al., 2013) are more likely to settle out of the water column during buoyant plume rise and remove isotopically light pFe to nearby sediments. An increase in δ^{56}TDFe with dispersion could theoretically be driven by the uptake and segregation of light isotopes from the plume by settling biogenic particles (Ellwood et al., 2015). We do not know the abundance or settling rates of such biogenic material in the water column at E2, but in the vent-proximal context of our plume samples, we expect the fraction of pFe associated with biogenic particles to be small compared to that of FeS$_2$ (Rouxel et al., 2016). Furthermore, FeS$_2$ is expected to settle more rapidly than biogenic material due its greater density, and therefore provides a more plausible means of segregating Fe isotopes from our closely spaced plume samples for ^{56}TDFe at E2.

The fraction of pFe present as sulphides and oxyhydroxides can be estimated from the relationship between pV/pFe and dissolved phosphate (Bennett et al., 2009) in order to re-construct how the change in sample composition influences δ^{56}TDFe. Dissolved phosphate scavenges onto Fe oxyhydroxides at constant molar ratios (Feely et al., 1996; Sands et al., 2012). The concentration of dissolved phosphate in the East Scotia Sea is 2.15 μM (Hawkes

et al., 2013). Using the linear relationship in Feely et al. (1998) an expected P/Fe ratio of 0.16 can be calculated. The inverse relationship between P/Fe and V/Fe in Feely et al. (1998) for Fe oxyhydroxide particles from different vents is used to calculate the expected pV/pFe for the Fe oxyhydroxide particles in the plume over Dog's Head. The fraction of Fe oxyhydroxide (pX_{FeOOH}) and Fe sulphide particles (pX_{FeS_2}) collected on filters is then calculated from Eqs. (2) and (3):

$$pX_{FeOOH} = (pV/pFe)_{measured}/(pV/pFe)_{expected} \qquad (2)$$

$$pX_{FeS_2} = 1 - pX_{FeOOH} \qquad (3)$$

As pX_{FeS_2} decreases and pX_{FeOOH} increases $\delta^{56}TDFe$ moves from $-0.31 \pm 0.03‰$ to $0.69 \pm 0.05‰$ with the exception of the two TDFe samples with the lightest $\delta^{56}TDFe$ (Fig. 6a dMn <2 nmol kg^{-1}), which are offset by the lightest $\delta^{56}dFe$ values. Samples taken in the black smoke of the hydrothermal plume using the ROV Isis had an average pX_{FeS_2} of 0.31 ± 0.03 ($n = 4$) (Table S4) when normalised to TDFe concentrations. This suggests that in the early stages of buoyant plume rise 31% of the Fe from the hydrothermal vent precipitates as FeS_2. Assuming that most of this FeS_2 is removed by settling to sediments, the isotopic fractionation can be calculated using the Fe isotope fractionation factor of $\alpha_{FeS-Fe(II)}$ 0.9992 from Butler et al. (2005). The removal of 31% of the initial TDFe in the vent fluid as FeS_2 would shift the vent proximal plume from $\delta^{56}TDFe$ $-0.31 \pm 0.03‰$ towards $\delta^{56}TDFe$ of 0.06‰. We find this predicted value to be broadly intermediate to the range of observed $\delta^{56}TDFe$ values in the buoyant plume ($-0.31 \pm 0.03‰$ to $0.78 \pm 0.05‰$) (Fig. 6b). In summary, the $\delta^{56}TDFe$ of the plume generally shifts towards heavier values, which are dependent on the balance between the amount of particulate FeS_2 and $FeOOH$. Isotopically light FeS_2 particles are denser than $FeOOH$ and therefore more likely to settle out of the water column faster as the plume is dispersed. As a result the $\delta^{56}TDFe$ of the plume becomes isotopically heavier relative to the vent source.

4.3. Isotope composition of dFe and effects of Fe oxyhydroxide precipitation

The presence of Fe oxyhydroxides in particulate samples (Eq. (2)) is used to evaluate controls on $\delta^{56}dFe$ in the buoyant plume during mixing and dispersal. Our buoyant plume samples will represent both lateral and vertical patchiness inherently attributed to the rapid and dynamically mixing plume environment. As such, even simple and well-defined reaction pathways are likely to be observed with a degree of scatter in vertical transects derived from in-situ hydrothermal plume sampling. Nonetheless, the wide range of pX_{FeOOH} (<0.05 to >0.95) indicates sampling by the ROV Isis successfully resolved the onset and almost full extent of particle formation and the corresponding influence on $\delta^{56}Fe$ during buoyant plume dispersal.

The decrease in $\delta^{56}dFe$ ($-0.41‰$ to $-1.98‰$) accompanied by increasing pX_{FeOOH} (Fig. 7) is consistent with the decreasing $\delta^{56}dFe$ during plume dispersal as described by dMn (Fig. 6b), where more dispersal equates to longer

timescales of oxidation and the formation of more Fe oxyhydroxides. We evaluate the trend in decreasing $\delta^{56}dFe$ using a Rayleigh equation and the $\alpha_{ferrihydrite-Fe(aq)}$ value of 1.0009 calculated from experiments by Bullen et al. (2001), and derive three mineral precipitation scenarios for comparison to our observations presented in Fig. 7.

$$\delta^{56}dFe = \delta^{56}vFe + \alpha_{ferrihydrite-Fe(aq)} \cdot \ln f dFe \qquad (4)$$

$$\delta^{56}dFe_{S_2} = \delta^{56}vFe_{-pFeS_2} + \alpha_{ferrihydrite-Fe(aq)} \cdot \ln f dFe \qquad (5)$$

$$\delta^{56}dFe = (\delta^{56}nanoFeS_2 \cdot f nanoFeS_2) + (\delta^{56}dFe_{S_2} \\ \cdot f dFe_{S_2}) \qquad (6)$$

In the first scenario (Eq. (4)), precipitation of Fe oxyhydroxides from the vent source ($\delta^{56}vFe$) provides a reasonable fit to the lower bounds of $\delta^{56}dFe$ observed (Fig. 7). The second scenario provides an improved fit to the observed data. In the second scenario $\delta^{56}vFe$ was partially (31%) precipitated as Fe sulphide which served to shift $\delta^{56}TDFe$ of the vent-proximal plume towards an isotopically heavier value of 0.06‰ ($\delta^{56}vFe_{-pFeS2}$) before the onset of Fe oxyhydroxide formation (Eqs. (5) and (S2)). These comparisons suggest that the early and partial removal of isotopically light dFe to Fe sulphides is needed to account for our observations of $\delta^{56}dFe$ at E2.

In the third scenario (Eq. (6)), we also consider the influence of FeS_2 nanoparticle formation and conservation in the plume, which might also be analogous to other kinetically stable forms of dFe. Scenario three assumes the same sulphide and oxyhydroxide reactions as scenario two. Fe isotopes are also fractionated as they are in scenario two, however, a portion of dFe is now present as stable FeS_2 nanoparticles ($fnanoFeS_2$) with a $\delta^{56}dFe$ between $-0.09‰$ and $-0.79‰$ ($\delta^{56}nanoFeS_2$). These values were chosen as $-0.09‰$ was the isotope composition calculated from mass balance of $\delta^{56}TDFe$ and $\delta^{56}dFe$ in the near vent sample where the pFe was entirely FeS_2 particles (Fig. 6a) and $-0.79‰$ the FeS_2 isotope composition expected from kinetic fractionation of the vent fluid end-member value of $-0.31‰$ with 31% pyrite formation. This range is within the breadth of $\delta^{56}Fe$ values measured for pyrite in high temperature and low temperature hydrothermal samples (Bennett et al., 2008; Rouxel et al., 2008). Given that the mechanics of FeS_2 nanoparticle formation are not fully understood this range covers the possibility that FeS_2 nanoparticles may have a $\delta^{56}Fe$ that reflects equilibrium fractionation as a result of formation at high temperature at the point of venting (Rouxel et al., 2008; Syverson et al., 2013) or a $\delta^{56}Fe$ that reflects low temperature kinetic fractionation (Bennett et al., 2009).

In scenario three (Eq. (6)), the fraction of dFe present as FeS_2 nanoparticles is set to increase from 1% to 99% with plume dilution to mimic the buoyant plume evolution as larger particles settle out of the water column. In the early stages of mixing, FeS_2 nanoparticles represent a small fraction of dFe ($fnanoFeS_2 = 1\%$ of dFe), but as Fe minerals continue to precipitate from the dFe pool and settle out of the plume, eventually only the stable FeS_2 nanoparticles remain ($fnanoFeS_2 = 99\%$ of dFe). The isotope composition predicted by scenario three forms an envelope which is

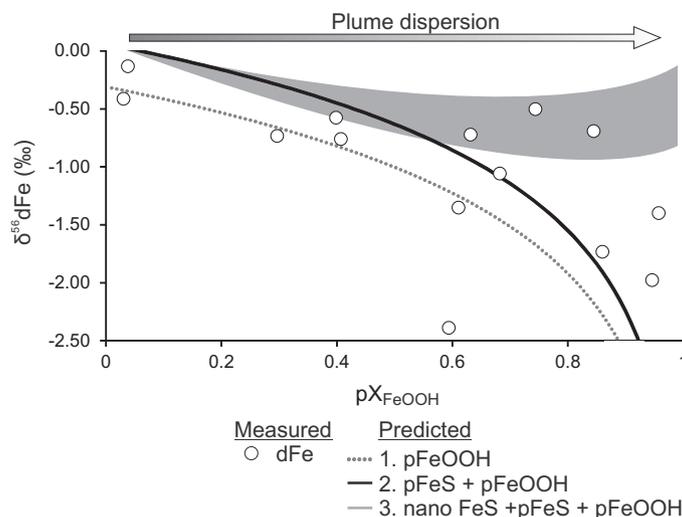Fig. 7. Isotope composition of dFe (circles) relative to the proportion of Fe oxyhydroxides (pX_{FeOOH}) in the particulate fraction. The evolution of the isotopic composition of dFe due to precipitation of different minerals is also plotted for comparison. Scenario 1 (grey dotted line) is the calculated Rayleigh fractionation curve for precipitation of dFe as Fe oxyhydroxide particles from a vent end-member $\delta^{56}TDFe$ of $-0.31‰$, and fractionation factor ($\alpha_{ferrihydrite-(aq)Fe}$) of 1.0009 from Bullen et al. (2001) (Eq. (4)). Scenario 2 (black solid line) is the same as 1 except a source composition of 0.06‰ that accounts for removal of 31% of the vent fluid Fe as FeS_2 particles (see Section 4.2) (Eqs. (5) and (S2)). Scenario 3 (grey shaded area) is calculated from mass balance assuming that Fe isotopes are fractionated the same as in scenario 2 but a fraction of dFe is present as stabilised dFe with an isotope composition of -0.09 to -0.79. Stabilised dFe is initially only 1% of dFe but as pX_{FeOOH} increases and dFe (III) is consumed by production of pFeOOH the inert stable dFe fraction increases to 99% of dFe (Eq. (6)). See Supplementary Information for full details.

isotopically heavier than most of the measured $\delta^{56}dFe$ values (Fig. 7), yet it provides a good description of the upper bounds of $\delta^{56}dFe$ values in the buoyant plume, and suggests the partial presence of FeS_2 nanoparticles may account for the deviations towards heavier values of $\delta^{56}dFe$ than predicted in scenario two. We therefore favour scenario 2 as the best explanation of Fe isotope fractionation in the plume with the caveat that deviations from this line maybe caused by the presence of stabilised forms of dFe, adsorption of dFe onto particles or biological Fe uptake. For a more detailed description of the fractionation scenarios the reader is referred to the Supplementary information.

Consistent with experimental work (Bullen et al., 2001; Welch et al., 2003; Butler et al., 2005) and the isotope composition of particulate Fe in hydrothermal plumes (Severmann et al., 2004; Bennett et al., 2009), our results show that Fe oxyhydroxide precipitation produces lighter values for residual $\delta^{56}dFe$, while the respective $\delta^{56}TDFe$ is isotopically heavier due to the preferential settling of isotopically light Fe sulphide minerals from the TDFe pool during plume dispersal (Fig. 6a and b). This means that after the isotope composition of the vent fluid is offset by FeS_2 precipitation, the isotope composition of dFe exported from the plume is largely dictated by the extent to which Fe oxyhydroxide particles form. Due to the amount of scatter in measured dFe isotope composition relative to the modelled fractionation curves it cannot be said definitively whether complexation of dFe by organic ligands or the formation of nanoparticles have an influence on $\delta^{56}dFe$. Based on the residuals of $\delta^{56}dFe$ relative to

calculated fractionation lines (scenario 1 and 2 in Fig. 7 and Fig. 4b), between 14% and 27% of the Fe isotope fractionation may result from the formation of nanoparticle/ligand complexed species and/or re-dissolution of particles relative to the overall effect from Fe oxyhydroxide and pyrite formation.

4.4. dFe exported to the neutrally buoyant plume and deep ocean

Trends in $\delta^{56}dFe$ in this study are best explained by precipitation of Fe sulphides and Fe oxyhydroxides in the buoyant plume (scenario two, Fig. 7). This suggests that the formation of Fe sulphide particles has an influence on the $\delta^{56}dFe$ of the hydrothermal plume at this location by immediately offsetting the $\delta^{56}Fe$ of the vent fluid source in the initial stages of plume rise.

By comparison the $\delta^{56}Fe$ of pFe in buoyant plumes studied previously ranges from $-0.31‰$ to $-0.7‰$ for pFe sourced from the Red Lion vent (Bennett et al., 2009) and 0.24–1.28‰ for pFe sourced from the Rainbow hydrothermal vent (Severmann et al., 2004). In both cases the $\delta^{56}pFe$ was heavier than the $\delta^{56}dFe$ measured in this study which is in the range $-0.13‰$ to $-2.39‰$. Red Lion and E2 can be compared directly due to the similarity in the isotope composition of the vent sources (E2 = $-0.31 \pm 0.03‰$ and Red Lion = $-0.29 \pm 0.05‰$).There was some overlap between the $\delta^{56}dFe$ results of this study and $\delta^{56}pFe$ measured by Bennett et al. (2009) but particles measured in their study covered a smaller range of pX_{FeOOH} from 0.34 to 0.69 whereas pX_{FeOOH} in this study ranged from 0.03

to 0.95. If δ^{56}pFe from Bennett et al. (2009) is compared to δ^{56}dFe from this study across the same range of pX$_{FeOOH}$ then the range of δ^{56}dFe is narrowed to −0.58‰ to −2.39‰, which is isotopically lighter than δ^{56}pFe in the Red Lion plume. This also suggests that when pX$_{FeOOH}$ is <0.34 the formation of Fe sulphides in the initial stage of plume dispersion will dominantly control the Fe isotope composition of dFe.

Bennett et al. (2009) also calculated δ^{56}dFe from mass balance using δ^{56}pFe and estimate that during buoyant plume dispersion δ^{56}dFe would increase from the vent fluid end-member of −0.29 ± 0.05 towards a value of 0.8 ± 2.2‰. These estimates are contrary to our results that show δ^{56}dFe getting isotopically lighter as the plume is dispersed and not heavier. The estimates made by Bennett et al. (2009) also assume that the δ^{56}TDFe of the plume remains constant during plume dispersion whereas our results show δ^{56}TDFe varies significantly in the buoyant plume most likely due to heterogeneous dispersion and settling of pFe. Hence, our observed δ^{56}dFe differ from the calculated δ^{56}dFe of Bennett et al. (2009).

A transect of δ^{56}dFe measurements reported values ranging from −0.92‰ to −1.35 ± 0.03‰ ($n = 5$) (Conway and John, 2014) in a hydrothermal plume over the TAG vent field, which was lighter than the TAG hydrothermal vent fluid δ^{56}dFe of −0.15 ± 0.03‰ ($n = 3$) (Severmann et al., 2004). These observations of isotopically light dFe are in agreement with our findings of isotopically light hydrothermal dFe relative to the bulk silicate earth. Our data shows a greater range of values than the ocean section data, due to the greater sampling resolution of the hydrothermal plume in this study where for δ^{56}dFe ($n = 17$). Using a mass balance approach and a hydrothermal plume end-member of −1.35‰ Conway and John (2014) estimate that 2.3% of dFe is derived from TAG in this N. Atlantic transect. The controls on plume Fe isotope fractionation revealed from the results presented in this study indicate that given the isotopically heavier vent fluid of TAG, the isotopically light hydrothermal plume end-member used to explain hydrothermal δ^{56}dFe in the N. Atlantic is the result of Fe oxyhydroxide precipitation in the buoyant plumes of the N. Atlantic (Conway and John, 2014).

The difference between the range of δ^{56}dFe from the E2 plume and the N. Atlantic (Conway and John, 2014) cannot be explained by differences in Fe/H$_2$S, (0.2 for E2 – Dogs Head and 1.5 for TAG) as higher Fe/H$_2$S for TAG should result in a larger portion of Fe precipitating as Fe oxyhydroxides, driving δ^{56}dFe towards values lighter than that of the E2 plume. Alternatively the difference in the range of δ^{56}dFe observed between the two sites could be explained by the higher Cu/Fe (0.028) and Zn/Fe (0.02) ratios in the Dogs Head vent fluid, relative to those of vents found on the MAR (0.005, 0.01 and 0.006–0.13) (German et al., 1991; Edmonds and German, 2004; Bennett et al., 2009). Lower concentrations of Cu and Zn in MAR vent fluids may result in more Fe sulphide precipitation in the overlying plume, which would shift the δ^{56}dFe exported from the buoyant plume towards heavier δ^{56}dFe values. In contrast, higher concentrations of Cu and Zn relative to Fe in vent

fluids from Dog's Head may result in less Fe sulphide precipitation and therefore, more Fe is converted to Fe oxyhydroxides resulting in a lighter δ^{56}dFe in the E2 plume. This suggests that differences in chemistry of vent fluids and Fe(II) oxidation rates in ocean basins influence the degree to which Fe isotopes are fractionated between pFe and dFe in plumes. This would result in unique Fe isotope signatures of dFe exported from hydrothermal plumes in different ocean basins. Therefore, it will be wise to consider the potential impact of other chalcophile elements competing for free sulphide, which may alter the pathways of authigenic Fe entrapment, when using Fe isotopes in the geological record to interpret past oceanic Fe cycling.

The δ^{56}dFe values of the E2 plume demonstrate that Fe isotopes in the hydrothermal plume are fractionated initially by precipitation of FeS$_2$ particles and subsequently by continual oxidation of Fe(II) to Fe(III) and the formation of Fe oxyhydroxides. Enclosing the plume samples within Niskin bottles is likely to slow Fe(II) oxidation compared to the in-situ plume but the aggregation of colloidal Fe oxyhydroxides may have been encouraged as the turbulent mixing of plume waters are continually dispersed in-situ making the aggregation of Fe oxyhydroxide colloids less likely. Based on the observations of how δ^{56}dFe is fractionated in samples, the in-situ Fe isotope composition of dFe exported to the NBP at E2 can be calculated from the measured δ^{56}TDFe of the vent proximal plume. Such a calculation uses known fractionation factors (Bullen et al., 2001; Butler et al., 2005), an estimated plume rise time and the calculated Fe(II) oxidation half-life (supplementary information Tables S1 and S4). The plume rise time is important as this dictates the amount of time for vent fluid Fe(II) to be oxidised to Fe(III) in the buoyant plume. Speer and Rona (1989) calculated that the rate of plume rise for both Pacific and Atlantic hydrothermal plumes was 0.1 m s^{-1} Assuming this is also the same at E2, which rises 245 m (Fig. 2), a rise time of 0.68 h can be estimated. Using the Fe(II) oxidation half time calculated for Scotia Sea deep water (1.38 h, supplementary information, Table S1) we calculate 71% of dFe may still be present as Fe(II) when the hydrothermal plume reaches a height of neutral buoyancy. If 31% of vent-derived dFe is precipitated as Fe sulphide particles during BP rise (as described in Section 4.2), a residual 69% of vent-derived dFe remains as dFe(II). From our Fe(II) NBP calculation 29% of the remaining vent derived dFe is oxidised to Fe(III) during plume rise a large fraction of which is removed from the dissolved fraction by formation of Fe oxyhydroxide particles with potentially a small amount persisting as colloids.

Using the Rayleigh equations and fractionation factors from scenario two (Fig. 7) we predict that the in-situ δ^{56}dFe supplied to the NBP will have a δ^{56}dFe composition of −0.28 ± 0.17‰ (represented schematically in Fig. 8). Our predicted δ^{56}dFe is similar to the δ^{56}TDFe of the vent proximal plume of −0.31 ± 0.03‰ as the processes of Fe sulphide and Fe oxyhydroxide formation have opposing, and in this instance, largely balanced effects during the course of BP dispersal. Such balanced isotope-fractionation processes may not occur in other ocean basins and at different vents where the extent of Fe sulphide and
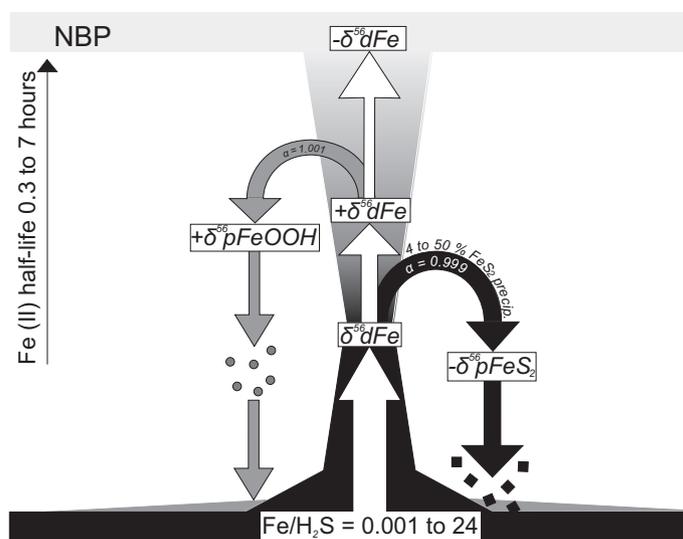
Fig. 8. Schematic diagram of Fe isotope fractionation described in text and Supplementary Information. Positive and negative signs indicate enrichment in the heavier or lighter Fe isotope. The range of Fe (II) half-lives represents the global range for different oceans basins as calculated by Field and Sherrell (2000). Shapes represent mineral particles of FeOOH (grey) and FeS$_2$ (black). Arrows with fractionation factors (α) are associated with mineral particles of the same colour. Fe/H$_2$S values represent the global range and the amount of FeS$_2$ precipitating is dependent on this (Mottl and McConachy, 1990; Rudnicki and Elderfield, 1993; Douville et al., 2002; Severmann et al., 2004; Bennett et al., 2009).

Fe oxyhydroxide formation will vary. Furthermore, continual physiochemical processing of iron in the NBP may impart further changes on the isotope composition of iron in the dissolved pool.

We consider the implications of Fe-sulphide and Fe-oxyhyoxide authigenesis on the dissolved iron isotope composition of other hydrothermal vents. Following our treatment of the E2 plume, the δ^{56}dFe of the NBP for Rainbow and TAG (N. Atlantic), Red Lion (S. Atlantic) and 9–10°N (E. Pacific) are estimated to be -1.37 ± 0.22‰, -0.73 ± 0.77‰, -0.30 ± 0.25‰, 0.36 ± 0.84‰ respectively. the similarity to their hydrothermal end-members of these estimates varies between sites (δ^{56}dFe of -0.14 ± 0.09‰, $n = 10$, -0.15 ± 0.07‰, $n = 3$ (Severmann et al., 2004); -0.29 ± 0.10‰, $n = 6$ (Bennett et al., 2009); -0.40 ± 0.14‰, $n = 7$ (Rouxel et al., 2008) (supplementary information, Table S4). These predicted NBP δ^{56}dFe may become isotopically lighter with continual aggregation of isotopically heavy colloidal Fe oxyhydroxides during long distance (1000's of km) export of the plume into the deep ocean.

Further, pronounced changes in the authigenic mineral sinks of Fe released from hydrothermal vents may have occurred during perturbations in ambient ocean redox chemistry of the past ocean. These changes may be reflected in the δ^{56}Fe of hydrothermal sediments.

5. CONCLUSIONS

Published studies of Fe isotopes in hydrothermal plumes have only determined the isotope composition of pFe, which is expected to eventually settle out of the water column to hydrothermal sediments. The conclusion of previous studies was that Fe isotopes are fractionated during particle precipitation in the dispersing plume, which alters the plume δ^{56}pFe relative to the hydrothermal source.

In this study the Fe isotope composition of both δ^{56}dFe, and δ^{56}TDFe fractions was determined and compared to the bulk chemical composition of Fe particles in order to assess the processes leading to Fe isotope fractionation in a hydrothermal plume. If the vent fluid source and local seawater values are well constrained, the isotopically light δ^{56}dFe signature of hydrothermal plumes can be used to trace hydrothermal input in different ocean basins.

Evidence for Fe isotope fractionation by Fe sulphide precipitation was only observed in δ^{56}TDFe samples that were isotopically heavier than the δ^{56}TDFe of the vent fluid source, indicating that a fraction of isotopically light pFe must have been removed from the plume, most likely by rapid settling of large Fe sulphide particles.

After an initial offset to heavier values in early plume mixing, the δ^{56}dFe decreased during buoyant plume rise to values isotopically lighter than the δ^{56}Fe of the hydrothermal vent source, with δ^{56}TDFe getting heavier with plume dispersion as a result of continuous particle precipitation. The shift to isotopically lighter δ^{56}dFe during further dispersion and aging of the plume can be explained by precipitation of Fe oxyhydroxides. The isotopically light δ^{56}dFe values presented here are in agreement with the basin scale studies of δ^{56}dFe (Conway and John, 2014) but they are not concordant with previous estimates of δ^{56}dFe calculated from plume mass balance and δ^{56}pFe (Bennett et al., 2009). This is because Bennett et al. (2009) base their prediction of δ^{56}dFe on the assumption that δ^{56}TDFe remains constant. Here we show that δ^{56}TDFe is highly variable due to complex mixing and settling of plume particles.

At the E2 hydrothermal site, δ^{56}dFe supplied to the neutrally buoyant plume has an inferred Fe isotope composition that is coincidentally isotopically similar to that of the initial hydrothermal vent fluid. If the balance of sulphide and oxide formation changes then the net impact on the iron isotope composition will shift accordingly. This study highlights the need to resolve Fe isotopes fractionation at the boundary between the ocean and Fe source regions as the isotope signature of the Fe exported from the source can be dramatically altered from its source isotope composition upon entering the ocean. This is an important consideration for the mass balance of Fe in the modern ocean and for using Fe isotopes to infer changes in the Fe cycle throughout past Earth history.

APPENDIX A. SUPPLEMENTARY DATA

Supplementary data associated with this article can be found, in the online version, at http://dx.doi.org/10.1016/j.gca.2016.12.022.

REFERENCES

Albarede F. and Beard B. (2004) Analytical methods for non-traditional isotopes. In *Geochemistry of Non-Traditional Stable Isotopes* (eds. C. M. Johnson, B. L. Beard and F. Albarede). Mineralogical Soc Amer, Chantilly, pp. 113–152.

Anbar A. D., Jarzecki A. A. and Spiro T. G. (2005) Theoretical investigation of iron isotope fractionation between $Fe(H_2O)_6^{3+}$ and $Fe(H_2O)_6^{2+}$: Implications for iron stable isotope geochemistry. *Geochim. Cosmochim. Acta* **69**, 825–837.

Beard B. L., Johnson C. M., Von Damm K. L. and Poulson R. L. (2003) Iron isotope constraints on Fe cycling and mass balance in oxygenated Earth oceans. *Geology* **31**, 629–632.

Bennett S. A., Achterberg E. P., Connelly D. P., Statham P. J., Fones G. R. and German C. R. (2008) The distribution and stabilisation of dissolved Fe in deep-sea hydrothermal plumes. *Earth Planet. Sci. Lett.* **270**, 157–167.

Bennett S. A., Rouxel O., Schmidt K., Garbe-Schonberg D., Statham P. J. and German C. R. (2009) Iron isotope fractionation in a buoyant hydrothermal plume, 5 degrees S Mid-Atlantic Ridge. *Geochim. Cosmochim. Acta* **73**, 5619–5634.

Biller D. V. and Bruland K. W. (2012) Analysis of Mn, Fe Co, Ni, Cu, Zn, Cd, and Pb in seawater using the Nobias-chelate PA1 resin and magnetic sector inductively coupled plasma mass spectrometry (ICP-MS). *Mar. Chem.* **130**, 12–20.

Bonnand P., Parkinson I. J., James R. H., Karjalainen A. M. and Fehr M. A. (2011) Accurate and precise determination of stable Cr isotope compositions in carbonates by double spike MC-ICP-MS. *J. Anal. At. Spectrom.* **26**, 528–535.

Bruguier N. J. and Livermore R. A. (2001) Enhanced magma supply at the southern East Scotia Ridge: evidence for mantle flow around the subducting slab? *Earth Planet. Sci. Lett.* **191**, 129–144.

Bullen T. D., White A. F., Childs C. W., Vivit D. V. and Schulz M. S. (2001) Demonstration of significant abiotic iron isotope fractionation in nature. *Geology* **29**, 699–702.

Butler I. B., Archer C., Vance D., Oldroyd A. and Rickard D. (2005) Fe isotope fractionation on FeS formation in ambient aqueous solution. *Earth Planet. Sci. Lett.* **236**, 430–442.

Carazzo G., Jellinek A. M. and Turchyn A. V. (2013) The remarkable longevity of submarine plumes: Implications for the hydrothermal input of iron to the deep-ocean. *Earth Planet. Sci. Lett.* **382**, 66–76.

Conway T. M. and John S. G. (2014) Quantification of dissolved iron sources to the North Atlantic Ocean. *Nature* **511**, 212–215.

Conway T. M., Rosenberg A. D., Adkins J. F. and John S. G. (2013) A new method for precise determination of iron, zinc and cadmium stable isotope ratios in seawater by double-spike mass spectrometry. *Anal. Chim. Acta* **793**, 44–52.

Cotte L., Waeles M., Pernet-Coudrier B., Sarradin P.-M., Cathalot C. and Riso R. D. (2015) A comparison of in situ vs. ex situ filtration methods on the assessment of dissolved and particulate metals at hydrothermal vents. *Deep Sea Res. Part I* **105**, 186–194.

Cowen J. P., Massoth G. J. and Feely R. A. (1990) Scavenging rates of dissolved manganese in a hydrothermal vent plume. *Deep Sea Res. Part A* **37**, 1619–1637.

Dauphas N., Pourmand A. and Teng F. Z. (2009) Routine isotopic analysis of iron by HR-MC-ICPMS: How precise and how accurate? *Chem. Geol.* **267**, 175–184.

Douville E., Charlou J. L., Oelkers E. H., Bienvenu P., Colon C. F. J., Donval J. P., Fouquet Y., Prieur D. and Appriou P. (2002) The rainbow vent fluids (36 degrees 14 ' N, MAR): the influence of ultramafic rocks and phase separation on trace metal content in Mid-Atlantic Ridge hydrothermal fluids. *Chem. Geol.* **184**, 37–48.

Edmonds H. N. and German C. R. (2004) Particle geochemistry in the Rainbow hydrothermal plume, Mid-Atlantic Ridge. *Geochim. Cosmochim. Acta* **68**, 759–772.

Elderfield H. and Schultz A. (1996) Mid-ocean ridge hydrothermal fluxes and the chemical composition of the ocean. *Annu. Rev. Earth Planet. Sci.* **24**, 191–224.

Ellwood M. J., Hutchins D. A., Lohan M. C., Milne A., Nasemann P., Nodder S. D., Sander S. G., Strzepek R., Wilhelm S. W. and Boyd P. W. (2015) Iron stable isotopes track pelagic iron cycling during a subtropical phytoplankton bloom. *Proc. Natl. Acad. Sci. U.S.A.* **112**, E15–E20.

Estapa M. L., Breier J. A. and German C. R. (2015) Particle dynamics in the rising plume at Piccard Hydrothermal Field, Mid-Cayman Rise. *Geochem. Geophys. Geosyst.* **16**, 2762–2774.

Feely R. A., Baker E. T., Marumo K., Urabe T., Ishibashi J., Gendron J., Lebon G. T. and Okamura K. (1996) Hydrothermal plume particles and dissolved phosphate over the superfast-spreading southern East Pacific Rise. *Geochim. Cosmochim. Acta* **60**, 2297–2323.

Feely R. A., Gendron J. F., Baker E. T. and Lebon G. T. (1994a) Hydrothermal plumes along the east pacific rise, 8-degrees-40' to 11-degrees-50'N - particle distribution and composition. *Earth Planet. Sci. Lett.* **128**, 19–36.

Feely R. A., Massoth G. J., Trefry J. H., Baker E. T., Paulson A. J. and Lebon G. T. (1994c) Composition and sedimentation of

hydrothermal plume particles from North Cleft Segment, Juan De Fuca Ridge. *J. Geophys. Res. Solid Earth* **99**, 4985–5006.

Feely R. A., Trefry J. H., Lebon G. T. and German C. R. (1998) The relationship between P/Fe and V/Fe ratios in hydrothermal precipitates and dissolved phosphate in seawater. *Geophys. Res. Lett.* **25**, 2253–2256.

Field M. P. and Sherrell R. M. (2000) Dissolved and particulate Fe in a hydrothermal plume at 9 degrees 45 ' N, East Pacific Rise: Slow Fe (II) oxidation kinetics in Pacific plumes. *Geochim. Cosmochim. Acta* **64**, 619–628.

Fitzsimmons J. N., Boyle E. A. and Jenkins W. J. (2014) Distal transport of dissolved hydrothermal iron in the deep South Pacific Ocean. *Proc. Natl. Acad. Sci. U.S.A.* **111**, 16654–16661.

Fitzsimmons J. N., Carrasco G. G., Wu J. F., Roshan S., Hatta M., Measures C. I., Conway T. M., John S. G. and Boyle E. A. (2015) Partitioning of dissolved iron and iron isotopes into soluble and colloidal phases along the GA03 GEOTRACES North Atlantic Transect. *Deep Sea Res. Part II* **116**, 130–151.

Gamo T., Ishibashi J., Tsunogai U., Okamura K. and Chiba H. (2006) Unique geochemistry of submarine hydrothermal fluids from arc-back-arc settings of the western pacific. In *Back-Arc Spreading Systems: Geological, Biological, Chemical, and Physical Interactions* (eds. D. M. Christie, C. R. Fisher, S. M. Lee and S. Givens). Amer Geophysical Union, Washington, pp. 147–161.

Gartman A., Findlay A. J. and Luther G. W. (2014) Nanoparticulate pyrite and other nanoparticles are a widespread component of hydrothermal vent black smoker emissions. *Chem. Geol.* **366**, 32–41.

German C. and Von Damm K. L. (2004) Hydrothermal processes. In *The Oceans and Marine Geochemistry. Treatise on Geochemistry* (ed. H. Elderfield). Elsevier-Pergamon, Oxford, pp. 182–216.

German C. R., Campbell A. C. and Edmond J. M. (1991) Hydrothermal scavenging at the Mid-Atlantic Ridge - modification of trace-element dissolved fluxes. *Earth Planet. Sci. Lett.* **107**, 101–114.

German C. R., Klinkhammer G. P. and Rudnicki M. D. (1996) The Rainbow hydrothermal plume, 36 degrees 15'N, MAR. *Geophys. Res. Lett.* **23**, 2979–2982.

German C. R., Legendre L. L., Sander S. G., Niquil N., Luther G. W., Bharati L., Han X. and Le Bris N. (2015) Hydrothermal Fe cycling and deep ocean organic carbon scavenging: Model-based evidence for significant POC supply to seafloor sediments. *Earth Planet. Sci. Lett.* **419**, 143–153.

German C. R., Livermore R. A., Baker E. T., Bruguier N. I., Connelly D. P., Cunningham A. P., Morris P., Rouse I. P., Statham P. J. and Tyler P. A. (2000) Hydrothermal plumes above the East Scotia Ridge: an isolated high-latitude back-arc spreading centre. *Earth Planet. Sci. Lett.* **184**, 241–250.

Hansen H. P. (2007) Determination of oxygen. In *Methods of Seawater Analysis* (eds. K. Grasshoff, K. Kremling and M. Ehrhardt). Wiley-VCH Verlag GmbH, Wiley Online Library, pp. 75–89.

Hawkes J. A., Connelly D. P., Gledhill M. and Achterberg E. P. (2013) The stabilisation and transportation of dissolved iron from high temperature hydrothermal vent systems. *Earth Planet. Sci. Lett.* **375**, 280–290.

Horner T. J., Williams H. M., Hein J. R., Saito M. A., Burton K. W., Halliday A. N. and Nielsen S. G. (2015) Persistence of deeply sourced iron in the Pacific Ocean. *Proc. Natl. Acad. Sci. U.S.A.* **112**, 1292–1297.

Icopini G. A., Anbar A. D., Ruebush S. S., Tien M. and Brantley S. L. (2004) Iron isotope fractionation during microbial reduction of iron: The importance of adsorption. *Geology* **32**, 205–208.

Ishibashi (1995) Backarc basins: tectonics and magmatism. In *Hydrothermal Activity Related to Arc-backarc Magmatism in the Western Pacific* (ed. B. Taylor). Plenum, NY, pp. 451–495.

James R. H. and Elderfield H. (1996) Dissolved and particulate trace metals in hydrothermal plumes at the Mid-Atlantic Ridge. *Geophys. Res. Lett.* **23**, 3499–3502.

James R. H., Green D. R. H., Stock M. J., Alker B. J., Banerjee N. R., Cole C., German C. R., Huvenne V. A. I., Powell A. M. and Connelly D. P. (2014) Composition of hydrothermal fluids and mineralogy of associated chimney material on the East Scotia Ridge back-arc spreading centre. *Geochim. Cosmochim. Acta* **139**, 47–71.

Johnson C. M., Beard B. L., Roden E. E., Newman D. K. and Nealson K. H. (2004) Isotopic constraints on biogeochemical cycling of Fe. In *Geochemistry of Non-Traditional Stable Isotopes* (eds. C. M. Johnson, B. L. Beard and F. Albarede). Mineralogical Soc America, Washington, pp. 359–408.

Kaeding J. (1973) W. Stumm und J. J. Morgan: Aquatic Chemistry An Introduction Emphasizing Chemical Equilibria in Natural Waters. New York, London, Sydney, Toronto, Wiley-Inter-science, 1970, 583 S., zahlr. Abb. und Tab. *Acta Hydroch. Hydrob.* **1**, 117.

Kagaya S., Maeba E., Inoue Y., Kamichatani W., Kajiwara T., Yanai H., Saito M. and Tohda K. (2009) A solid phase extraction using a chelate resin immobilizing carboxymethylated pentaethylenehexamine for separation and preconcentration of trace elements in water samples. *Talanta* **79**, 146–152.

Kleint C., Hawkes J. A., Sander S. G. and Koschinsky A. (2016) Voltammetric investigation of hydrothermal iron speciation. *Front. Mar. Sci.* **3**.

Klunder M. B., Laan P., Middag R., de Baar H. J. W. and Bakker K. (2012) Dissolved iron in the Arctic Ocean: Important role of hydrothermal sources, shelf input and scavenging removal. *J. Geophys. Res. C: Oceans* **117**, 17.

Klunder M. B., Laan P., Middag R., De Baar H. J. W. and van Ooijen J. C. (2011) Dissolved iron in the Southern Ocean (Atlantic sector). *Deep Sea Res. Part II* **58**, 2678–2694.

Lacan F., Radic A., Jeandel C., Poitrasson F., Sarthou G., Pradoux C. and Freydier R. (2008) Measurement of the isotopic composition of dissolved iron in the open ocean. *Geophys. Res. Lett.* **35**, 5.

Lacan F., Radic A., Labatut M., Jeandel C., Poitrasson F., Sarthou G., Pradoux C., Chmeleff J. and Freydier R. (2010) High-precision determination of the isotopic composition of dissolved iron in iron depleted seawater by double spike multicollector-ICPMS. *Anal. Chem.* **82**, 7103–7111.

Lemaitre N., Bayon G., Ondréas H., Caprais J.-C., Freslon N., Bollinger C., Rouget M.-L., de Prunelé A., Ruffine L., Olu-Le Roy K. and Sarthou G. (2014) Trace element behaviour at cold seeps and the potential export of dissolved iron to the ocean. *Earth Planet. Sci. Lett.* **404**, 376–388.

Levasseur S., Frank M., Hein J. R. and Halliday A. (2004) The global variation in the iron isotope composition of marine hydrogenetic ferromanganese deposits: implications for seawater chemistry? *Earth Planet. Sci. Lett.* **224**, 91–105.

Li M., Toner B. M., Baker B. J., Breier J. A., Sheik C. S. and Dick G. J. (2014) Microbial iron uptake as a mechanism for dispersing iron from deep-sea hydrothermal vents. *Nat. Commun.* **5**, 8.

Loscher B. M., DeBaar H. J. W., DeJong J. T. M., Veth C. and Dehairs F. (1997) The distribution of Fe in the Antarctic Circumpolar Current. *Deep Sea Res. Part II* **44**, 143–187.

Martin J. H. (1990) Glacial-interglacial CO_2 change: the iron hypothesis. *Paleoceanography* **5**, 1–13.

McDuff R. E. (1995) Physical dynamics of deep sea hydrothermal plumes. In *Saefloor Hydrothermal Systems: Physical, Chemical,*

Biological and Geological Interactions (eds. S. E. Humphris, R. A. Zierenberg, L. S. Mullineaux and R. E. Thomson). American Geophysical Union, Washington, DC.

Mikutta C., Wiederhold J. G., Cirpka O. A., Hofstetter T. B., Bourdon B. and Von Gunten U. (2009) Iron isotope fractionation and atom exchange during sorption of ferrous iron to mineral surfaces. *Geochim. Cosmochim. Acta* **73**, 1795–1812.

Millero F. J., Sotolongo S. and Izaguirre M. (1987) The oxidation kinetics of Fe(II) in seawater. *Geochimica et Cosmochimica Acta* **51**, 793–801.

Milne A., Landing W., Bizimis M. and Morton P. (2010) Determination of Mn, Fe Co, Ni, Cu, Zn, Cd and Pb in seawater using high resolution magnetic sector inductively coupled mass spectrometry (HR-ICP-MS). *Anal. Chim. Acta* **665**, 200–207.

Moore C. M., Mills M. M., Arrigo K. R., Berman-Frank I., Bopp L., Boyd P. W., Galbraith E. D., Geider R. J., Guieu C., Jaccard S. L., Jickells T. D., La Roche J., Lenton T. M., Mahowald N. M., Maranon E., Marinov I., Moore J. K., Nakatsuka T., Oschlies A., Saito M. A., Thingstad T. F., Tsuda A. and Ulloa O. (2013) Processes and patterns of oceanic nutrient limitation. *Nat. Geosci.* **6**, 701–710.

Mottl M. J. and McConachy T. F. (1990) Chemical processes in buoyant hydrothermal plumes on the East Pacific Rise near 21°N. *Geochim. Cosmochim. Acta* **54**, 1911–1927.

Naveira Garabato A. C., McDonagh E. L., Stevens D. P., Heywood K. J. and Sanders R. J. (2002) On the export of antarctic bottom water from the Weddell Sea. *Deep Sea Res. Part II* **49**, 4715–4742.

Nishioka J., Obata H. and Tsumune D. (2013) Evidence of an extensive spread of hydrothermal dissolved iron in the Indian Ocean. *Earth Planet. Sci. Lett.* **361**, 26–33.

Poitrasson F. and Freydier R. (2005) Heavy iron isotope composition of granites determined by high resolution MC-ICP-MS. *Chem. Geol.* **222**, 132–147.

Polyakov V. B., Clayton R. N., Horita J. and Mineev S. D. (2007) Equilibrium iron isotope fractionation factors of minerals: Reevaluation from the data of nuclear inelastic resonant X-ray scattering and Mossbauer spectroscopy. *Geochim. Cosmochim. Acta* **71**, 3833–3846.

Resing J. A., Sedwick P. N., German C. R., Jenkins W. J., Moffett J. W., Sohst B. M. and Tagliabue A. (2015) Basin-scale transport of hydrothermal dissolved metals across the South Pacific Ocean. *Nature* **523**, U140–U200.

Revels B. N., Ohnemus D. C., Lam P. J., Conway T. M. and John S. G. (2015) The isotopic signature and distribution of particulate iron in the North Atlantic Ocean. *Deep Sea Res. Part II* **116**, 321–331.

Rogers A. D., Tyler P. A., Connelly D. P., Copley J. T., James R., Larter R. D., Linse K., Mills R. A., Garabato A. N., Pancost R. D., Pearce D. A., Polunin N. V., German C. R., Shank T., Boersch-Supan P. H., Alker B. J., Aquilina A., Bennett S. A., Clarke A., Dinley R. J., Graham A. G., Green D. R., Hawkes J. A., Hepburn L., Hilario A., Huvenne V. A., Marsh L., Ramirez-Llodra E., Reid W. D., Roterman C. N., Sweeting C. J., Thatje S. and Zwirglmaier K. (2012) The discovery of new deep-sea hydrothermal vent communities in the southern ocean and implications for biogeography. *PLoS Biol.* **10** e1001234.

Rouxel O., Shanks W. C., Bach W. and Edwards K. J. (2008) Integrated Fe- and S-isotope study of seafloor hydrothermal vents at East Pacific rise 9–10 degrees N. *Chem. Geol.* **252**, 214–227.

Rouxel O., Toner B. M., Manganini S. J. and German C. R. (2016) Geochemistry and iron isotope systematics of hydrothermal plume fall-out at East Pacific Rise 9°50′N. *Chem. Geol.* **441**, 212–234.

Rudnicki M. D. and Elderfield H. (1993) A chemical-model of the buoyant and neutrally buoyant plume above the TAG vent field, 26 degrees-N, Mid-Atlantic Ridge. *Geochim. Cosmochim. Acta* **57**, 2939–2957.

Sands C. M., Connelly D. P., Statham P. J. and German C. R. (2012) Size fractionation of trace metals in the Edmond hydrothermal plume, Central Indian Ocean. *Earth Planet. Sci. Lett.* **319**, 15–22.

Schwertmann U., Friedl J. and Stanjek H. (1999) From Fe(III) Ions to Ferrihydrite and then to Hematite. *J. Colloid Interface Sci.* **209**, 215–223.

Sedwick P. N., Sohst B. M., Ussher S. J. and Bowie A. R. (2015) A zonal picture of the water column distribution of dissolved iron (II) during the U.S. GEOTRACES North Atlantic transect cruise (GEOTRACES GA03). *Deep Sea Res. Part II* **116**, 166–175.

Severmann S., Johnson C. M., Beard B. L., German C. R., Edmonds H. N., Chiba H. and Green D. R. H. (2004) The effect of plume processes on the Fe isotope composition of hydrothermally derived Fe in the deep ocean as inferred from the Rainbow vent site, Mid-Atlantic Ridge, 36°14′N. *Earth Planet. Sci. Lett.* **225**, 63–76.

Sharma M., Polizzotto M. and Anbar A. D. (2001) Iron isotopes in hot springs along the Juan de Fuca Ridge. *Earth Planet. Sci. Lett.* **194**, 39–51.

Skulan J. L., Beard B. L. and Johnson C. M. (2002) Kinetic and equilibrium Fe isotope fractionation between aqueous Fe(III) and hematite. *Geochim. Cosmochim. Acta* **66**, 2995–3015.

Speer K. G. and Rona P. A. (1989) A model of an Atlantic and Pacific hydrothermal plume. *J. Geophys. Res. C: Oceans* **94**, 6213–6220.

Syverson D. D., Borrok D. M. and Seyfried W. E. (2013) Experimental determination of equilibrium Fe isotopic fractionation between pyrite and dissolved Fe under hydrothermal conditions. *Geochim. Cosmochim. Acta* **122**, 170–183.

Tagliabue A. et al. (2010) Hydrothermal contribution to the oceanic dissolved iron inventory. *Nature* **3**, 252–256.

Teutsch N., von Gunten U., Porcelli D., Cirpka O. A. and Halliday A. N. (2005) Adsorption as a cause for iron isotope fractionation in reduced groundwater. *Geochim. Cosmochim. Acta* **69**, 4175–4185.

Toner B. M., Fakra S. C., Manganini S. J., Santelli C. M., Marcus M. A., Moffett J., Rouxel O., German C. R. and Edwards K. J. (2009) Preservation of iron(II) by carbon-rich matrices in a hydrothermal plume. *Nat. Geosci.* **2**, 197–201.

Trefry J. H. and Metz S. (1989) Role of hydrothermal precipitates in the geochemical cycling of Vanadium. *Nature* **342**, 531–533.

Von Damm K. L., Edmond J. M., Grant B. and Measures C. I. (1985) Chemistry of submarine hydrothermal solutions at 21-degrees-N, East Pacific Rise. *Geochim. Cosmochim. Acta* **49**, 2197–2220.

Walter H. J., Hegner E., Diekmann B., Kuhn G. and van der Loeff M. M. R. (2000) Provenance and transport of terrigenous sediment in the South Atlantic Ocean and their relations to glacial and interglacial cycles: Nd and Sr isotopic evidence. *Geochim. Cosmochim. Acta* **64**, 3813–3827.

Welch S. A., Beard B. L., Johnson C. M. and Braterman P. S. (2003) Kinetic and equilibrium Fe isotope fractionation between aqueous Fe(II) and Fe(III). *Geochim. Cosmochim. Acta* **67**, 4231–4250.

Wu J. F., Wells M. L. and Rember R. (2011a) Dissolved iron anomaly in the deep tropical-subtropical Pacific: Evidence for long-range transport of hydrothermal iron. *Geochim. Cosmochim. Acta* **75**, 460–468.

Wu L. L., Beard B. L., Roden E. E. and Johnson C. M. (2011b) Stable iron isotope fractionation between aqueous Fe(II) and hydrous ferric oxide. *Environ. Sci. Technol.* **45**, 1847–1852.

Yucel M., Gartman A., Chan C. S. and Luther G. W. (2011) Hydrothermal vents as a kinetically stable source of iron-sulphide-bearing nanoparticles to the ocean. *Nat. Geosci.* **4**, 367–371.

Associate editor: Frederic Moynier